Finite Slip Models of the 2019 Ridgecrest Earthquake Sequence Constrained by Space Geodetic Data and Aftershock Locations

Zeyu Jin*[1] and Yuri Fialko[1]

ABSTRACT

The July 2019 Ridgecrest, California, earthquake sequence involved two large events—the M 6.4 foreshock and the M 7.1 mainshock that ruptured a system of intersecting strike-slip faults. We present analysis of space geodetic observations including Synthetic Aperture Radar and Global Navigation Satellite System data, geological field mapping, and seismicity to constrain the subsurface rupture geometry and slip distribution. The data render a complex pattern of faulting with a number of subparallel as well as cross-cutting fault strands that exhibit variations in both strike and dip angles, including a "flower structure" formed by shallow splay faults. Slip inversions are performed using both homogeneous and layered elastic half-space models informed by the local seismic tomography data. The inferred slip distribution suggests a moderate amount of the shallow coseismic slip deficit. The peak moment release occurred in the depth interval of 3–4 km, consistent with results from previous studies of major strike-slip earthquakes, and the depth distribution of seismicity in California. We use the derived slip models to investigate stress transfer and possible triggering relationships between the M 7.1 mainshock and the M 6.4 foreshock, as well as other moderate events that occurred in the vicinity of the M 7.1 hypocenter. Triggering is discouraged for the average strike of the M 7.1 rupture (320°) but encouraged for the initial orientation of the mainshock rupture suggested by the first-motion data (340°). This lends support to a scenario according to which the earthquake rupture nucleated on a small fault that was more optimally oriented with respect to the regional stress and subsequently propagated along the less-favorably oriented pre-existing faults, possibly facilitated by dynamic weakening. The nucleation site of the mainshock experienced positive dynamic Coulomb stress changes that are much larger than the static stress changes, yet the former failed to initiate rupture.

KEY POINTS

- Slip models are constrained by a joint analysis of surface displacements and seismicity data.
- The M 6.4 foreshock promoted nucleation of the mainshock on a plane suggested by the first *P*-wave arrivals.
- Slip averaged along the rupture has a maximum amplitude at depth of 3–4 km, similar to other M 7 events.

Supplemental Material

INTRODUCTION

The 2019 Ridgecrest, California, earthquake sequence initiated on 4 July with a strong M_w 6.4 foreshock followed by an M_w 7.1 mainshock on 5 July. The M_w 7.1 (hereafter, we drop the subscript w and refer to the earthquake magnitude as to the moment magnitude, unless otherwise noted) mainshock was the largest event that struck California over the last 20 yr, since the 1999 Hector Mine earthquake (Barnhart *et al.*, 2019; Liu *et al.*, 2019; Ross *et al.*, 2019; Chen *et al.*, 2020). The epicentral area of the 2019 earthquake sequence is located between the town of Ridgecrest to the southwest, the Searles Valley to the east, and the Garlock fault to the south (Fig. 1). Faults that produced the foreshock and the mainshock, as well as their numerous aftershocks, were not previously recognized as continuous connected features capable of producing a major earthquake, but appear to be spatially associated with the Little Lake fault zone. The latter is in turn part of the eastern California shear zone (ECSZ), a complex network of active

1. University of California, Institute of Geophysics and Planetary Physics, Scripps Institution of Oceanography, La Jolla, California, U.S.A.

*Corresponding author: zej011@ucsd.edu

Cite this article as Jin, Z., and Y. Fialko (2020). Finite Slip Models of the 2019 Ridgecrest Earthquake Sequence Constrained by Space Geodetic Data and Aftershock Locations, *Bull. Seismol. Soc. Am.* **110**, 1660–1679, doi: 10.1785/0120200060

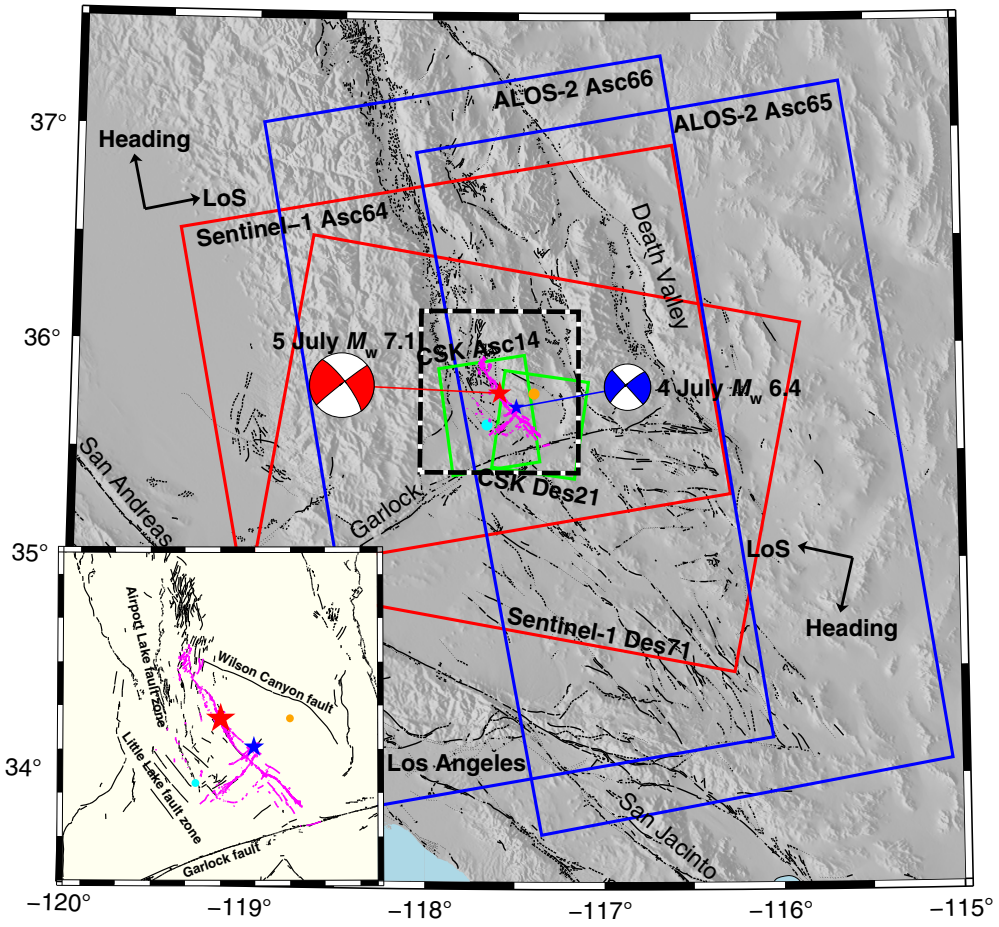

Figure 1. Regional map of the study area. Magenta lines denote surface offsets due to the Ridgecrest earthquakes mapped by field surveys (Ponti *et al.*, 2020). Red and blue stars denote the epicenters of M 7.1 and M 6.4 earthquakes, and red and blue "focal mechanism plots" denote the respective focal mechanisms. The red, blue, and green polygons represent swaths of Synthetic Aperture Radar data from Sentinel-1, Advanced Land Observation Satellite (ALOS)-2 and Cosmo-Skymed satellite missions used in this study. Arrows show the satellite heading (azimuth) and look (range) direction for the ascending and descending satellite orbits. Black wavy lines denote mapped active faults (Jennings and Bryant, 2010). Cyan and orange dots denote the towns of Ridgecrest and Searles Valley, respectively. (Inset) A close-up view of the earthquake area outlined by the dashed rectangle. CSK, Cosmo-SkyMed. The color version of this figure is available only in the electronic edition.

Quaternary faults that accommodates between 10% and 20% of the relative motion between the Pacific and North American plates (Sauber *et al.*, 1986; Dokka and Travis, 1990; McClusky *et al.*, 2001; Tymofyeyeva and Fialko, 2015). It has been proposed that the ECSZ represents an incipient plate boundary forming in response to the development of a major restraining bend in the San Andreas fault system to the west (Nur *et al.*, 1993). Indeed, all of the major (M 7+) earthquakes that occurred in southern California over the last 50 yr were located in the ECSZ (e.g., Sieh *et al.*, 1993; Fialko *et al.*, 2001; Hauksson *et al.*, 2002; Simons *et al.*, 2002; Fialko, 2004).

The M 6.4 foreshock activated a left-lateral northeast-trending fault and possibly a 10–20-kilometer-long segment of a right-lateral northwest-trending fault that was subsequently ruptured by the M 7.1 mainshock (e.g., Ross *et al.*, 2019). The mainshock nucleated ~15 km to the northwest of the foreshock epicenter and bilaterally propagated along a system of previously mapped and unmapped right-lateral faults striking northwest. Most of the M 7.1 rupture occurred within the boundaries of the U.S. Naval Air Weapons Station at China Lake. The most recent (prior to 2019) activity in the Ridgecrest area involved a series of moderate to strong earthquakes in 1995–1996 (Hauksson *et al.*, 1995), some of which occurred within just a few kilometers from the epicenter of the mainshock of the 2019 sequence. This clustering of seismic activity, combined with large volumes of high-quality observations, makes the Ridgecrest sequence a good target for investigations aimed at improving our understanding of the mechanisms of spatiotemporal earthquake clustering, stress-mediated earthquake interaction, and triggering. In this article, we use a rich combination of space geodetic, geologic, and seismic observations to derive finite slip models of the 2019 foreshock–mainshock sequence. We then apply these models to investigate the role of static and dynamic stress changes and stress heterogeneity in the earthquake triggering.

DATA AND METHODS

The 2019 Ridgecrest earthquakes occurred in the middle of dense instrumental networks, including the Plate Boundary Observatory (PBO; Herring *et al.*, 2016), and the Southern California Seismic Network (Hauksson *et al.*, 2001). They were also well imaged by a number of currently active satellite missions with Interferometric Synthetic Aperture Radar (InSAR) capabilities, including C-band Sentinel-1A/B, L-band Advanced Land Observation Satellite (ALOS)-2, and X-band Cosmo-Skymed (see Fig. 1 for data coverage). This, together with nearly optimal surface conditions for InSAR (arid semi-desert with sparse vegetation) and a rapid field response

TABLE 1
Synthetic Aperture Radar Data Used in This Study

Heading Track Number	Interferometric Pairs (yyyy/mm/dd)	Time Span (days)	Satellites*	$B_\perp$ (m)†
Descending 71	2019/07/04–2019/07/16	12	Sentinel-1	29.7
Descending 21	2019/06/27–2019/07/13	16	Cosmo-Skymed	176.2
Ascending 64	2019/07/04–2019/07/10	16	Sentinel-1	126.6
Ascending 14	2019/07/04–2019/07/20	16	Cosmo-Skymed	452.4
Ascending 65	2016/08/08–2019/07/08	1064	ALOS-2	2.4
Ascending 66	2017/08/12–2019/07/13	700	ALOS-2	14.6

Spatial coverage of each data set is shown in Figure 1. ALOS, Advanced Land Observation Satellite.
*The resolution of Sentinel-1 range offsets is 2.3 m, and the resolution of Cosmo-Skymed azimuth offsets is 2.2 m.
†Smaller perpendicular baselines ($B_\perp$) and larger radar wavelengths result in a better correlation of the radar phase (Rosen *et al.*, 1996).

including geologic, geodetic, and seismic components, resulted in a comprehensive data set that makes the 2019 Ridgecrest earthquake sequence one of the best-documented seismic events to date. Large volumes of high-quality data enable modeling of the earthquake sources with increasing accuracy and resolution. In this section, we describe the data sets that were used to inform our models of the Ridgecrest earthquakes.

Synthetic Aperture Radar data

High-quality Synthetic Aperture Radar (SAR) data from different look directions are in principle sufficient to completely describe surface displacements due to large shallow earthquakes (e.g., Fialko, 2004; Fialko *et al.*, 2001; Fialko, Sandwell, *et al.*, 2005). Such data were acquired over the Ridgecrest area shortly before and after the foreshock–mainshock sequence by a number of satellite missions (Fig. 1). Because the two largest events occurred within just one day of each other, the timing of SAR acquisitions allows measurements of combined displacements from the M 6.4 and M 7.1 events, and not from either event individually. In the Stress Changes due to the M 6.4 Foreshock and Possible Triggering of the M 7.1 Mainshock section, we show that it may be possible to separate contributions to surface deformation from the foreshock and the mainshock, given a well-resolved slip model for the composite event.

SAR data that most tightly bracket the earthquake dates were acquired by the Sentinel-1A and 1B satellites of the European Space Agency (see Table 1 and red frames in Fig. 1). Sentinel-1A/B satellites operate using C-band (radar wavelength of 56 mm) in the Terrain Observation by Progressive Scan (TOPS) mode, which allows for wide (~250 km) swaths and short (minimum of six day) repeat intervals. Image pairs that span the earthquake dates are available from both the ascending and descending satellite orbits, providing different look directions, and a complete coverage of an area around the earthquake ruptures and beyond (Fig. 1). A comparable coverage is also provided by the ALOS-2 mission of the Japanese Space Agency (Fig. 1, blue frames) that operates in the Scanning Synthetic Aperture Radar mode on the ascending tracks. ALOS-2 uses an L-band radar (wavelength of 0.24 m) that can provide a better coherence compared with C-band in areas affected by decorrelation (e.g., due to vegetation or intense damage near the surface rupture). We did not find this to be the case for the Ridgecrest sequence, possibly because the effect of a larger wavelength was offset by longer revisit intervals (Table 1), resulting in larger temporal decorrelation (e.g., Ahmed *et al.*, 2011).

Even though the ALOS-2 interferograms do not provide an increased diversity in look directions compared with the Sentinel-1 data, the former are useful in that they are affected by errors (mostly, the propagation delays) that are independent from those in the Sentinel-1 data. We complement the Sentinel-1 and ALOS-2 observations with SAR data from the Cosmo-Skymed satellites that operate in stripmap mode using X-band (wavelength of 31 mm). Because of the limited swath width and relatively sparse acquisitions, the Cosmo-Skymed data provide only a partial coverage of the rupture area (Fig. 1, green frames) and are highly affected by decorrelation of the radar phase. However, a smaller pixel size, especially in the azimuth direction (by almost an order of magnitude, compared with Sentinel-1 and ALOS-2 data), makes the Cosmo-Skymed data useful for constraining the north–south component of the coseismic displacement field that is not well resolved by the Sentinel-1 and ALOS-2 measurements.

To minimize possible contributions from postseismic deformation (Johnson *et al.*, 2006; Barbot, Hamiel, and Fialko, 2008; Gonzalez-Ortega *et al.*, 2014; Wang and Fialko, 2014, 2018), we considered postearthquake scenes that were acquired within 20 days after the mainshock. Analysis of the near-field Global Navigation Satellite System (GNSS) data indicated that postseismic displacements did not exceed a few tens of millimeters in the months following the earthquakes (Floyd *et al.*, 2020) and are therefore negligible compared with the coseismic displacements. The preseismic scenes were chosen to minimize the time span and perpendicular baselines of the coseismic pairs. The resulting data set is summarized in Table 1.

All interferometric pairs were processed using GMTSAR (an open source InSAR processing system with Generic Mapping Tools) (Sandwell *et al.*, 2011). The topography contribution

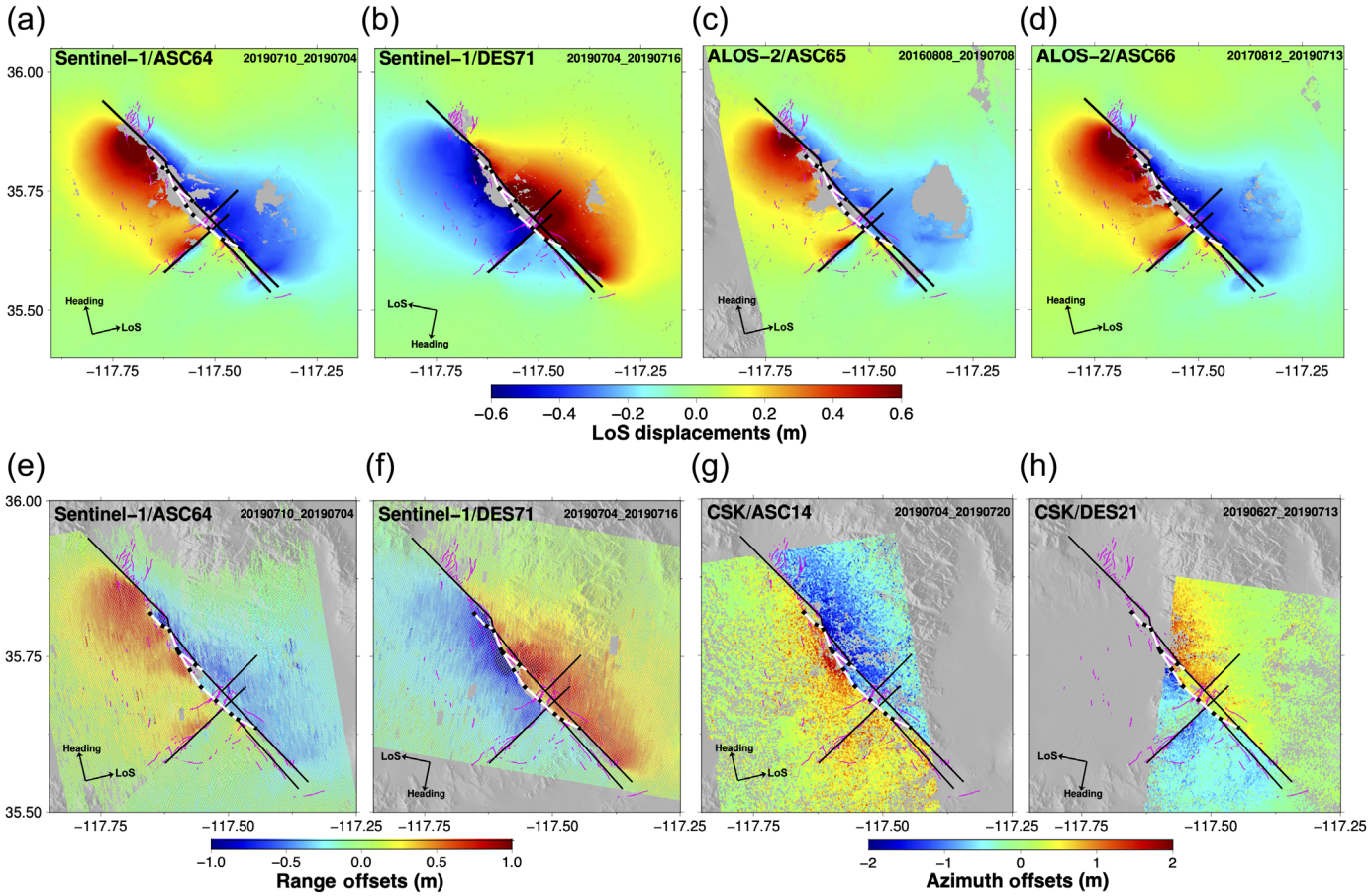

Figure 2. (a–d) Line-of-sight (LoS) displacements from Sentinel-1 interferograms from the (a) ascending and (b) descending tracks, and ALOS-2 interferograms from (c,d) two ascending tracks. (e,f) Range offsets from the Sentinel-1 data (same pairs as in panels (a,b)). (g,h) Azimuth offsets from the Cosmo-Skymed data. Positive LoS displacements correspond to motion toward the satellite. Black lines represent a piecewise linear approximation of the rupture trace based on all available data (interferograms, range and azimuth offsets, seismicity, and field data). Solid black lines denote subvertical faults that extend throughout the seismogenic layer, and dotted black and white lines denote surface traces of shallow splay faults. Magenta lines indicate rupture traces mapped by field surveys. The color version of this figure is available only in the electronic edition.

to the radar phase was calculated and removed using digital elevation data from the Shuttle Radar Topography Mission with 30 m resolution (Farr and Kobrick, 2000). The images were coregistered using a geometric alignment. Even in case of a perfect alignment, meter-scale surface displacements near the earthquake rupture introduce phase discontinuities across the burst boundaries in Sentinel-1 interferograms. Because the observed phase discontinuities across the burst boundaries are small, here we simply neglect them. In general, such discontinuities can be removed using a coseismic model to compute a range- and azimuth-dependent alignment, similar to corrections for the ionospheric perturbations (e.g., Wang *et al.*, 2017).

To avoid artifacts due to unwrapping errors in the near field of the earthquake ruptures (where the decorrelation noise can be large), we unwrapped the radar phase using a conservative branch-cut algorithm (Goldstein *et al.*, 1988). The resulting line-of-sight (LoS) displacements are shown in Figure 2a–d. To quantify surface displacements in the near field of the earthquake ruptures where the radar phase cannot be confidently unwrapped due to decorrelation, we computed range offsets using Sentinel-1 data (Fig. 2e,f), and azimuth offsets using Cosmo-Skymed data (Fig. 2g,h). Although the offsets are less accurate compared with the differential radar phase, they are useful for locating the rupture and constraining the distribution of slip in the shallow crust. Because the azimuth pixel size for Sentinel-1 TOPS mode is almost an order of magnitude larger than the range pixel size, the Sentinel-1 azimuth offsets have a low signal-to-noise ratio (SNR) and are not used for slip inversions. We performed a quality check on all of the scenes used in the inversions and manually masked out a few areas that were strongly affected by local errors or noise.

GNSS data

The Ridgecrest earthquakes occurred in an area spanned by the PBO, a mature network of continuously recording GNSS sites. This gave rise to a large set of well-constrained vector coseismic displacements. However, because the average spacing between

continuous GNSS (cGNSS) sites of PBO is on the order of 10–20 km, the cGNSS data primarily constrain integral characteristics of seismic sources such as the moment tensor and/or the scalar moment. To densify the GNSS coverage in the near field, teams from the University of California, San Diego, University of California at Riverside, University of Nevada at Reno, and the U.S. Geological Survey coordinated a postevent response to occupy existing geodetic benchmarks within ~50 km from the earthquake rupture. Most of the selected benchmarks have been surveyed multiple times over the last 30 yr, and some were surveyed as recently as several months prior to the July 2019 earthquakes (Floyd *et al.*, 2020). We have collected postevent data from seven campaign sites: 0806, INYO, GS11, GS17, GS20, GS22, and GS48. Some of the surveyed sites had benchmarks consisting of metal rods driven or cemented into the ground, with center markings, that required a tripod setup (Fig. 3a). At other sites, benchmarks consisted of a threaded pin encastered in a concrete block. For such sites, a GNSS antenna can be attached directly to a pin, without the need for a tripod (Fig. 3b).

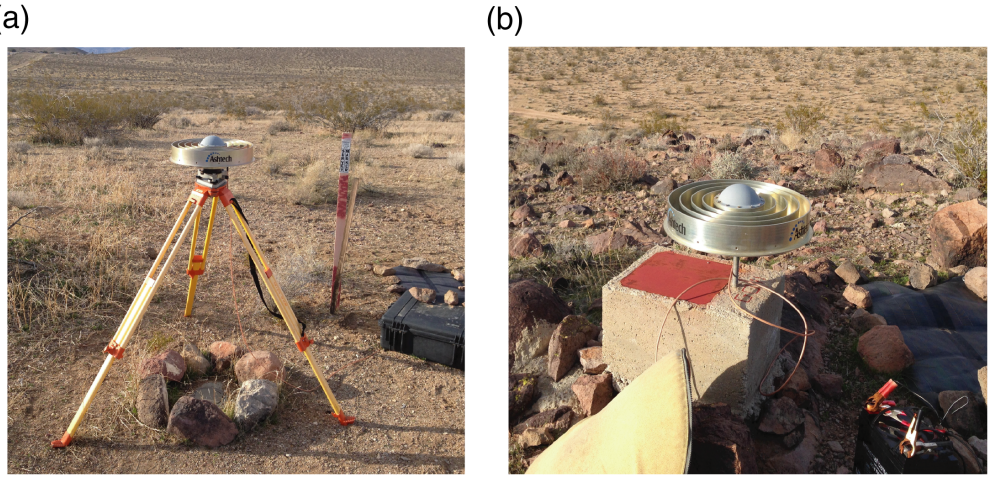

Figure 3. (a) Campaign site 0806; (b) campaign site GS11. The color version of this figure is available only in the electronic edition.

The data were collected at 15 s sampling intervals, and RINEX files were archived at UNAVCO (Fialko, Sandwell, *et al.*, 2019). Following the postevent deployment, we left the sites running to document the early postseismic deformation transient (Fialko, Jin, Tymofyeyeva, and Floyd, 2019). Solutions for coseismic displacements derived from the campaign GNSS measurements were presented in Floyd *et al.* (2020). We use the coseismic offsets derived from campaign as well as cGNSS data (Floyd *et al.*, 2020), along with data described in the SAR Data section in joint inversions for the static slip models, as described in the Joint Inversions of Surface Displacement Data section.

JOINT INVERSIONS OF SURFACE DISPLACEMENT DATA

To prepare the InSAR data for inversions for the subsurface slip distribution, we detrended the interferograms using low-resolution inverse models. A wide-swath capability of Sentinel-1 and ALOS-2 ensures that coseismic interferograms extend into areas where coseismic displacements are negligible (Fig. 1). The satellite orbits are known sufficiently well such that the orbital errors should not introduce significant long-wavelength trends in the data. However, we find that the long-wavelength trends are often present, possibly due to propagation effects (e.g., regional variations in the troposphere and/or ionosphere) and need to be accounted for. Even in the absence of the long-wavelength artifacts, one needs to estimate the phase ambiguity corresponding to the far-field ("zero") displacements. We do so by performing inversions for the slip distribution and the best-fitting linear (or, in case of ALOS-2, higher order) ramps in the radar phase using coarsely discretized fault models and coseismic interferograms (e.g., Fialko, 2004). In these preliminary inversions, we limited the fault depth to 15 km, based on the depth distribution of seismicity (e.g., Ross *et al.*, 2019) to avoid trade-offs between spurious deep slip and the ramp coefficients, and assigned relatively heavy weights to the cGNSS data. The best-fit ramps were subtracted from the radar interferograms. Because the range offsets represent the same projection of the surface displacement field as the radar interferograms, we detrended the range offsets by fitting a linear ramp to the residual between the detrended radar interferograms and the offsets, for each of the satellite tracks. The estimated ramps were subtracted from the range offsets, so that the latter have the same asymptotic behavior in the far field as the detrended interferograms and the cGNSS data. The azimuth offsets from Cosmo-Skymed were not included in the initial inversions because of a narrow swath that may not extend into a region of vanishing coseismic displacements (Fig. 1). Detrending of the azimuth offsets was performed at the next stage using a refined slip model. The azimuth offsets thus provide independent constraints only on the shallow (depth <5 km) part of the slip model, as intended.

The detrended interferograms and range and azimuth offset maps were subsampled using a quad-tree algorithm (Jonsson *et al.*, 2002; Simons *et al.*, 2002). To avoid oversampling in areas affected by high-frequency noise (atmospheric contributions, unwrapping errors, phase decorrelation, and so forth),

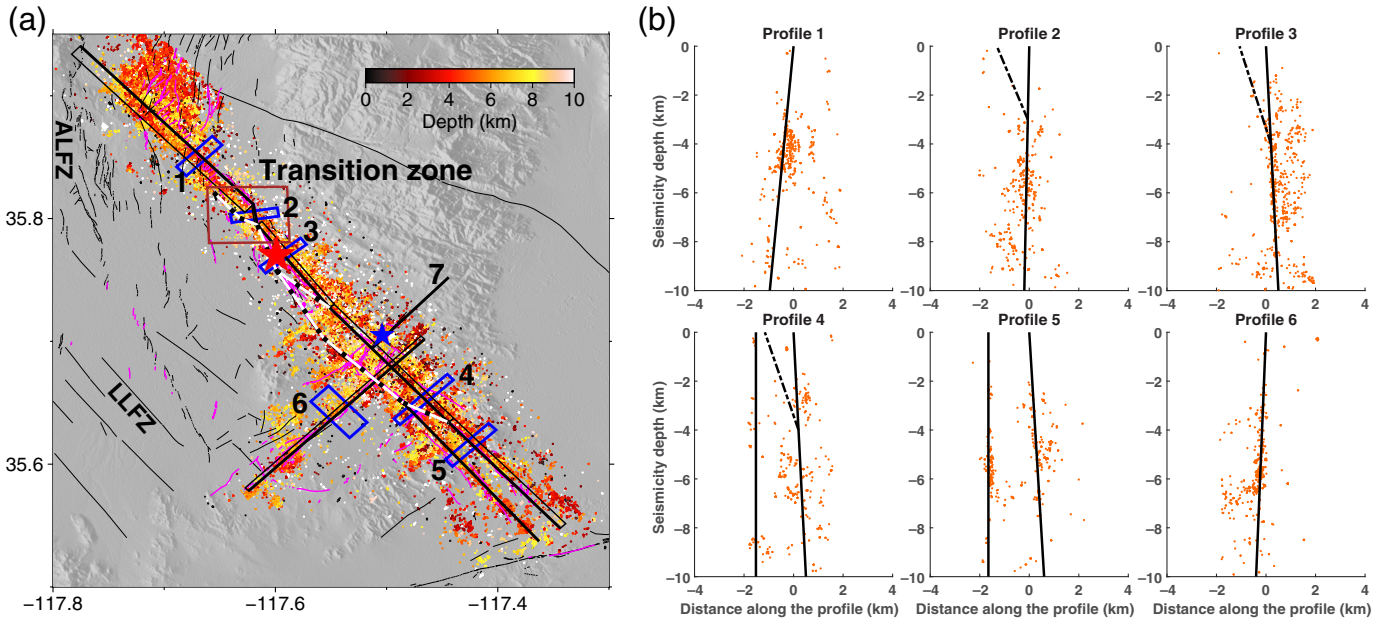

Figure 4. (a) Map view of aftershocks produced by the Ridgecrest events. Color dots represent the aftershock epicenters, color-coded by depth. Magenta lines represent surface traces of the 2019 earthquakes (Ponti *et al.*, 2020), and black lines represent Quaternary faults (Jennings and Bryant, 2010). Solid and dotted black lines denote surface traces of modeled fault planes. Solid thin rectangles correspond to fault planes that extend to the bottom of the seismogenic zone, and dotted lines correspond to shallow splay faults. Epicenters of the M 6.4 and M 7.1 events are indicated by blue and red stars (same as in Fig. 2). Blue rectangles correspond to the cross-section profiles shown in (b). Area of diffuse seismicity at the northern end of the M 7.1 rupture is truncated at 5 km from the fault trace. ALFZ, Airport Lake fault zone; LLFZ, Little Lake fault zone. (b) Seismicity distribution and locations of the modeled fault segments in several cross sections across the fault trace; see the respective profiles in (a). Dashed lines denote the splay faults that connect surface offsets to seismicity that starts at depth of 3–4 km. The down-dip extent of aftershocks is ∼10 km. The color version of this figure is available only in the electronic edition.

we downsampled the data iteratively using model predictions (Wang and Fialko, 2015). Following an initial inversion in which the best-fit slip model was obtained, the location of the data samples was determined by executing the gradient-based quad-tree algorithm on a model prediction. The obtained resolution cells were populated by the mean values of data from the original detrended interferograms. Usually, two or three iterations are sufficient to achieve a convergent set of data points. To capture the details of slip distribution near the Earth's surface, we more densely sampled the offsets data around the fault traces. In particular, given the patch size of ∼1 km at the shallowest part of the slip model, we sampled the near-field data starting with the minimum resolution cell of ∼250 m. The (spatially variable) unit look vectors for all data samples were computed by averaging the original values in the same resolution cells as used for subsampling the displacement data.

The subsurface fault geometry is typically not well known and is usually either assumed or estimated as part of a nonlinear inversion of surface displacement data (e.g., Simons *et al.*, 2002; Fialko, 2004). However, in case of the Ridgecrest earthquakes, data from a dense seismic network and advanced processing algorithms provided a catalog of accurately located aftershocks (e.g., Ross *et al.*, 2019) that can be used to infer the rupture geometry throughout the seismogenic zone, under the assumption that aftershocks are illuminating the ruptured faults and/or their immediate neighborhood. We approximate the ruptures that produced the M 6.4 foreshock and the M 7.1 mainshock by a set of rectangular fault segments that honor multiple available data sets, including the aftershock locations (Ross *et al.*, 2019), geologically mapped fault traces (Ponti *et al.*, 2020), and surface offsets from the space geodetic imaging (Fig. 2). The inferred geometry is illustrated in Figure 4 (also see Figs. S3 and S4, available in the supplemental material to this article).

Notable features of the aftershock distribution are: (1) change in the dip angle around the epicenter of the M 7.1 event, with a steep southwest dip in the northern part of the rupture, and a northeast dip in the southern part; (2) two subparallel northwest-trending strands of seismicity in the southern section; and (3) clear offsets between the surface rupture trace and the projection of the aftershock cloud toward the surface in the central part of the rupture (shown by the dotted and solid black lines in Fig. 4a, respectively). We interpret this offset as a shallow splay structure that connects the surface rupture to the main fault strand at depth that is expressed in the aftershock activity (Fig. 4b). The shallow-dipping splay fault is not expressed in microseismicity, as is the "main" rupture in the shallow crust, presumably because of the velocity-strengthening

conditions at low temperature and normal stress (e.g., Rice and Tse, 1986; Marone and Scholz, 1988; Barbot, Fialko, and Bock, 2009; Mitchell *et al.*, 2016). As we show later, the shallow splay structure has nevertheless produced a large coseismic offset. The data shown in Figure 4 also suggest that except for numerous cross faults, the northwest-striking fault at depth is quite linear and exhibits less variability in strike compared with the surface expression of the earthquake rupture.

We extended the rectangular segments approximating the fault geometry to the depth of 25 km, and by several kilometers beyond the mapped fault traces along strike, and subdivided each segment into slip patches of which sizes gradually increase from about 1 km (along-strike and down-dip) at the top of the fault to about 5–10 km at the bottom, following a geometric progression to ensure that the model resolution does not decrease with depth (Fialko, 2004). We computed Green's functions for the strike and dip components of slip on each patch for every observation point. As there are many more data points than the degrees of freedom, the system is overdetermined and is solved by minimizing the L_2 norm of the residual. We applied a positivity constraint on strike-slip components, such that no slip on the northeast-trending segments was allowed to be right lateral, and no slip on the northwest-trending segments was allowed to be left lateral. No positivity constraints were imposed on the dip-slip components, but the latter were more strongly smoothed compared with the strike-slip components to avoid spatially oscillating slip patterns. The first-order Tikhonov regularization (e.g., Golub *et al.*, 1999) was applied to avoid extreme variations in slip between the adjacent fault patches. This also refers to complex intersections between different fault segments (e.g., between the shallow splay faults and the main fault), in which case the "neighboring" patches were identified based on a distance between the patch edges.

We further regularized the problem by imposing "soft" zero-slip boundary conditions ($wS = 0$, in which S is an unknown slip magnitude, and w is a prescribed weight) at the fault edges, except for most of the edges at the free surface that were left unconstrained. Although the solution does not exhibit artifacts without a zero-slip boundary condition (e.g., no spurious large slip at the distant edges of the fault model), the latter helps ensure a well-behaved asymptotic decay of slip away from the source region. We also applied a soft zero-slip boundary condition at some segments of the fault trace at the surface where the data do not show a displacement discontinuity (e.g., on the eastern branch of the M 7.1 rupture just east of the epicenter). This helps prevent a spurious shallow slip due to smoothness constraints on the slip distribution and relatively sparse subsampled points, as the displacement gradients across a "blind" fault trace may be relatively small (e.g., Wang and Fialko, 2015). The optimal values of the smoothness parameters and the relative weighting of different data sets (Sentinel-1, ALOS-2, Cosmo-Skymed, cGNSS and campaign GNSS) used in the inversion were determined using the Chi-Squared statistics (see Fig. S1). We point out that although the regularization using smoothness constraints may appear as a somewhat arbitrary mathematical cure to the ill-conditioned nature of inverse problems, it does serve a purpose of discriminating against solutions that violate physical constraints such as the finite-fault strength. Under a typical set of assumptions about the data and the model parameters, a Tikhonov-type regularization yields results that are similar to those obtained using the Bayesian inference methods that are, however, much more computationally expensive (e.g., Bishop, 1995; Vogel, 2002).

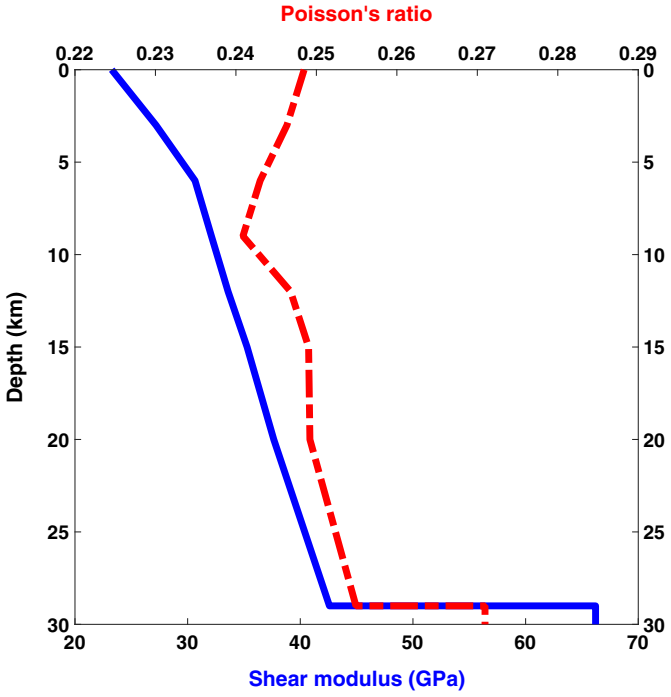

Figure 5. Variations in the elastic shear modulus (blue line, bottom axis) and Poisson's ratio (dashed red line, top axis) as a function of depth, as inferred from the seismic velocity model of Zhang and Lin (2014). The color version of this figure is available only in the electronic edition.

We performed two sets of inversions, one using Green's functions for a homogeneous elastic half-space (Okada, 1985) and another for a layered elastic half-space (Wang *et al.*, 2003). For the latter, we computed elastic moduli from the 3D seismic tomography models of the Ridgecrest area (Hauksson and Unruh, 2007; Zhang and Lin, 2014). Although the data in principle allow one to compute Green's functions for an elastic half-space with a 3D distribution of elastic moduli (e.g., Barbot, Fialko, and Sandwell, 2009), the predicted deformation due to fault slip is mostly sensitive to variations in the elastic moduli with depth, as variations in the lateral direction are relatively minor. The average 1D elastic rigidity structure used in our models is shown in Figure 5. For the sake of consistency, we adopted the same fault geometry in the homogeneous

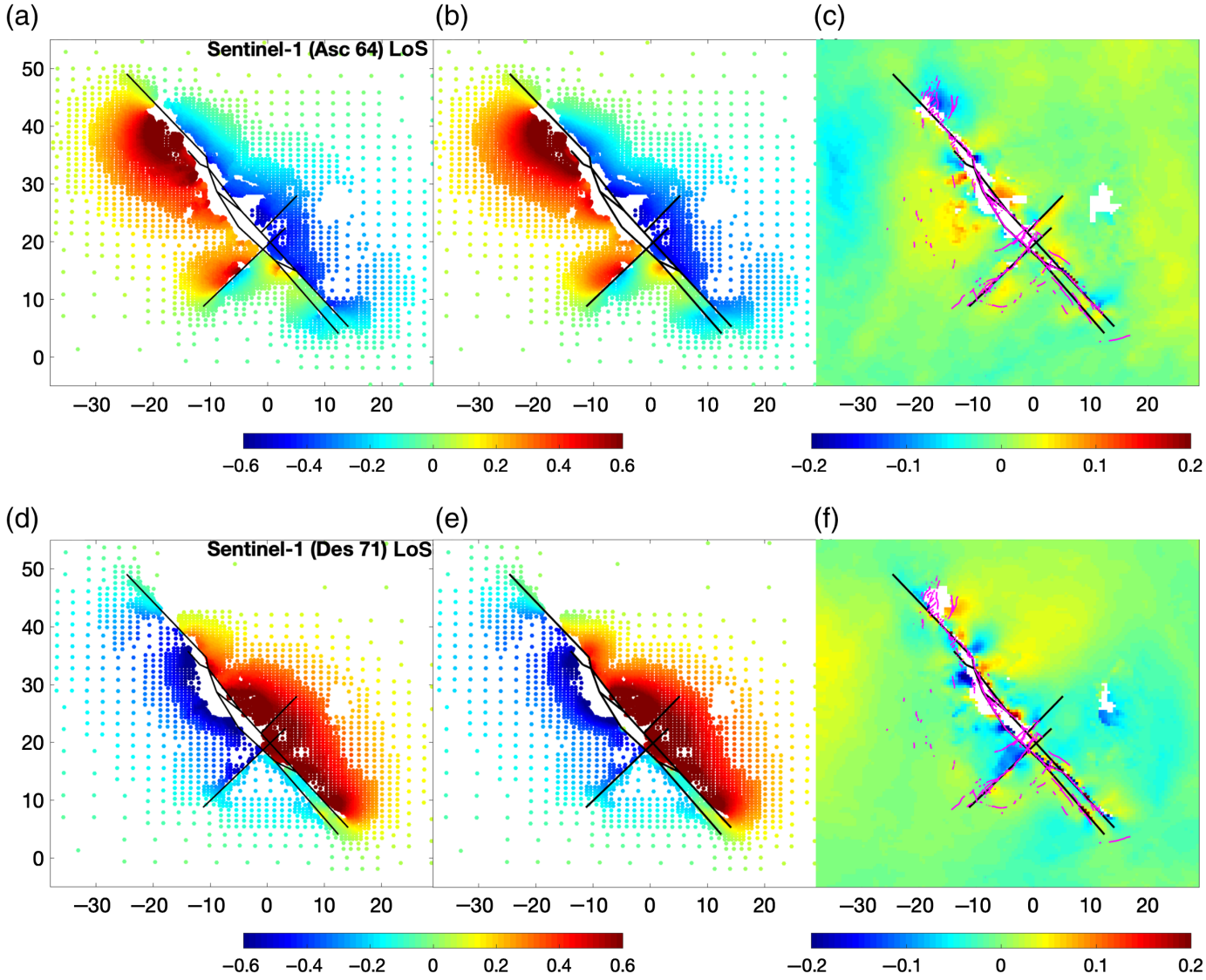

Figure 6. (a,d) Subsampled data, (b,e) best-fitting models, and (c,f) residuals for the Sentinel-1 radar interferograms from the (a–c) ascending track 64 and (d–f) descending track 71. Colors denote the amplitude of LoS displacements, in meters. Motion toward the satellite is deemed positive. Horizontal and vertical axes are in UTM coordinates (eastings and northings, respectively), in kilometers, with respect to a local origin (117.5° W, 35.5° N). The color version of this figure is available only in the electronic edition.

and layered half-space models. In case of the layered models, rectangular fault patches were approximated by a superposition of point sources.

In addition to solving for the slip distribution given the assumed fault geometry, we performed inversions using a grid search in which the dip angles of various fault segments were allowed to vary. Results of these inversions are presented in Figures S2 and S5, and, in general, lend support to the fault geometry constrained by the aftershock data (Fig. 4).

BEST-FIT MODELS: RESULTS

Figure 6 shows the subsampled data points, predictions of the best-fit models, and residuals (the difference between the data and the model predictions) for the Sentinel-1 interferograms from the ascending and descending tracks. We compute residuals at the original (unsampled) resolution to illustrate the model fit to all of the data points, including those that were not used in the inversion. Overall, the model fits the main features of the displacement field quite well, with the variance reduction of more than 94%. Most of the misfit is concentrated near the rupture trace, where the assumption of elastic deformation off of the fault plane is likely violated (e.g., Kaneko and Fialko, 2011). Figure 7 shows the model fit to the Sentinel-1 range offsets. Model fits to the ALOS-2 and Cosmo-Skymed data are presented in Figures S6 and S7. A comparison with other proposed models of the Ridgecrest earthquakes shows that our model is able to explain the data reasonably well (Wang *et al.*, 2020).

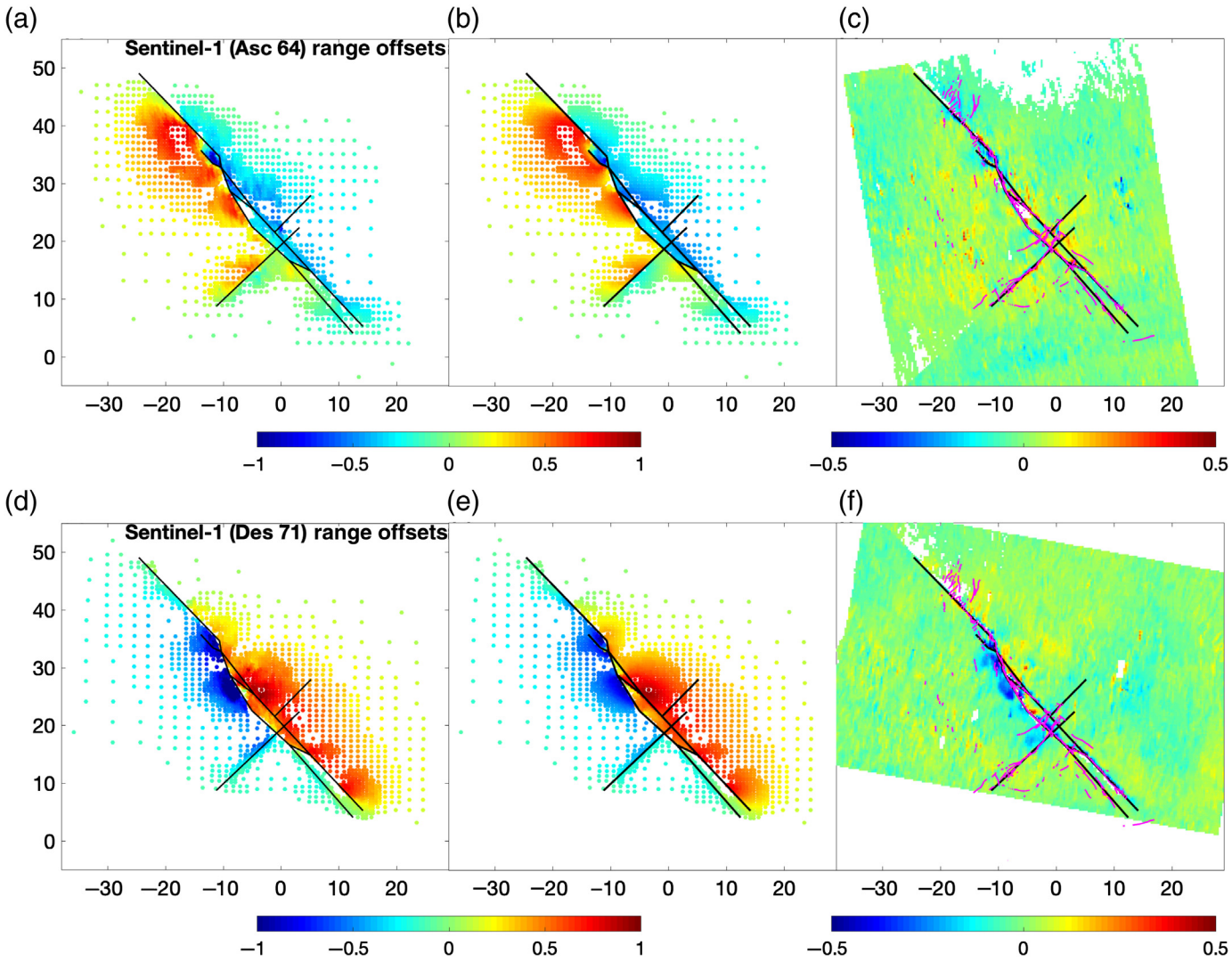

Figure 7. (a,d) Subsampled data, (b,e) best-fitting models, and (c,f) residuals for the Sentinel-1 range offsets from the (a–c) ascending track 64 and (d–f) descending track 71. Colors denote the amplitude of range offsets, in meters. Other notation is the same as in Figure 6. The color version of this figure is available only in the electronic edition.

Figure 8 shows the observed and modeled horizontal displacements at the cGNSS and campaign GNSS sites. We find that models that provide a good fit to the SAR data (provided the latter are available from a diverse set of look angles) are able to accurately "postdict" the independent GNSS data. The GNSS data, therefore, do not need to be heavily weighted in the joint inversions. The GNSS data are, however, quite useful for estimating and removing the long-wavelength trends and the "zero displacement" uncertainty in the LoS displacements, as discussed in the SAR Data section. As one can see in Figure 8, our best-fit model renders a good agreement with the GNSS data, particularly in case of cGNSS (Fig. 8a). For the campaign data, the fit is also adequate for sites that experienced large coseismic displacements. Sites with small displacements (and thus reduced SNR) render a poorer fit, in particular, because many of the sites had the most recent occupation 15–20 yr ago, so there is a large uncertainty in extrapolating the preseismic velocity (Floyd *et al.*, 2020). Cyan triangles in Figure 8b denote campaign sites at which data were collected shortly after the July 2019 events, but not included in the inversion. In particular, we excluded sites at which the angle between the observed and modeled horizontal displacements exceeded 45° (GS04 and GS25), or the magnitude of the observed and modeled horizontal displacements differed by more than a factor of 2 (GS16). For site GS20, no coseismic solution is available, as the early postearthquake data were corrupted because of a receiver malfunction.

Figures 9 and 10 show the slip distribution for the best-fit models, assuming the homogeneous and layered elastic half-space, respectively. As expected, the slip distributions look similar; the main difference is that the slip is somewhat shallower and, on average, smaller in case of a homogeneous half-space compared with a layered half-space (e.g., Fialko, 2004). Tests

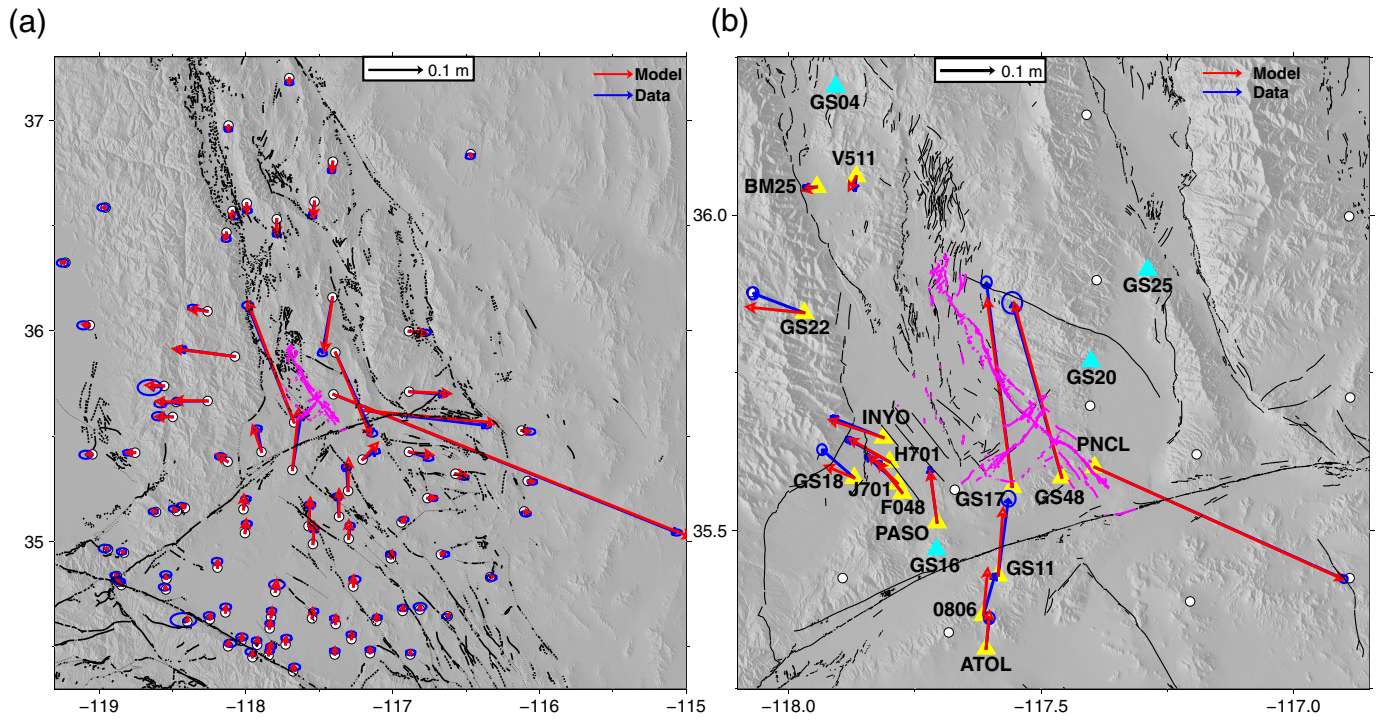

Figure 8. (a) Observed (blue arrows) and modeled (red arrows) horizontal coseismic displacements at the continuous Global Navigation Satellite System (cGNSS sites; white circles) of the Plate Boundary Observatory network. The ellipses show the 2σ errors. (b) Same as in (a), for the campaign Global Navigation Satellite System (GNSS) sites (yellow triangles). Cyan triangles denote campaign sites at which data was collected, but not used in the inversions due to quality issues. White circles denote the location of the cGNSS sites. Solutions for the coseismic offsets are from Floyd *et al.* (2020). The color version of this figure is available only in the electronic edition.

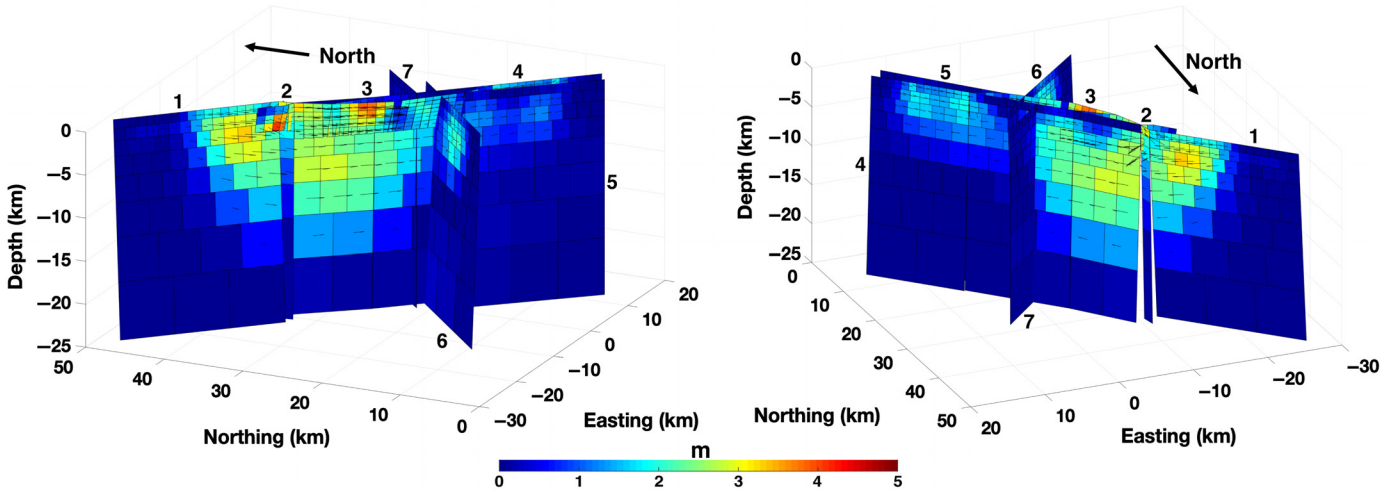

Figure 9. Slip distribution from the joint inversion of space geodetic data using a homogeneous elastic half-space model. Colors denote the total amplitude of slip, and arrows show the direction of slip. The two panels represent perspectives from different vantage points. The calculated geodetic moment magnitude for the mainshock is M 7.03. The color version of this figure is available only in the electronic edition.

using synthetic data indicate that the model resolution is not strongly dependent on depth (see Fig. S9).

We evaluate the "geodetic" moment magnitude $M_g = 2/3(\log_{10} GP - 9.1)$, in which $G = 33$ GPa is the nominal shear modulus, and P is the seismic potency, computed as an algebraic sum $\Sigma_{i=1}^{N} A_i S_i$, in which N is the number of slip patches (dislocations), and A_i and S_i are the area of, and the amplitude of slip on, patch i. Our models (Figs. 9 and

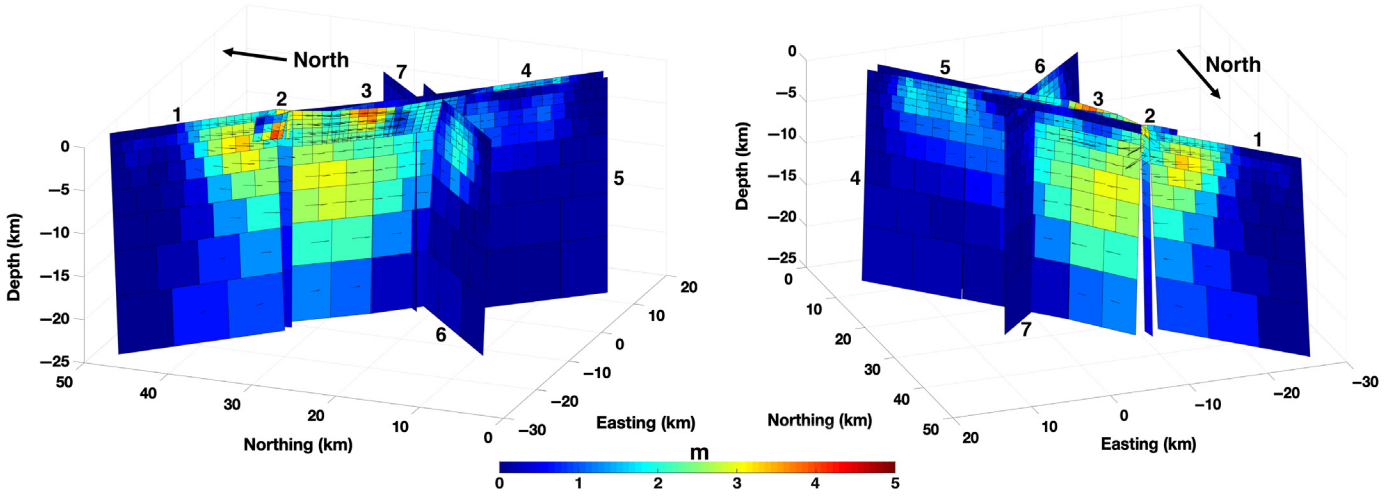

Figure 10. Slip distribution from the joint inversion of space geodetic data using a layered elastic half-space model. Notation is the same as in same as Figure 9. The calculated geodetic moment magnitude for the mainshock is M 7.10. The color version of this figure is available only in the electronic edition.

10) correspond to a composite event consisting of the foreshock and the mainshock. Assuming that the foreshock was dominated by slip on the left-lateral faults 6 and 7, and the mainshock was dominated by slip on the right-lateral faults 1–5 (see Fig. 4 for the segment numbers), we estimate M_g of 6.42 for the foreshock and 7.03 for the mainshock, in case of the homogeneous half-space model. In case of the layered half-space model, the respective values of the geodetic moment magnitude are 6.46 and 7.10. Thus, the geodetic moments inferred from inversions of static displacements are in a good agreement with the seismic moments derived from the waveform spectra (see Data and Resources). This is similar to findings from previous studies of large events for which high-quality data are available (e.g., Simons *et al.*, 2002; Fialko, 2004; Fialko, Sandwell, *et al.*, 2005; Barbot, Hamiel, and Fialko, 2008; Barbot, Fialko, and Bock, 2009; Wang and Fialko, 2018). In addition to providing a better agreement with the seismic data, more complex (and presumably more realistic) layered models appear to be more consistent with certain features of the geodetic data. Although the homogeneous and layered half-space models, on average, fit the geodetic data equally well, we find that the layered models do a better job fitting the far-field decay of the coseismic displacements (Fig. S8).

Apart from cross faults that persist throughout the seismogenic layer (Ross *et al.*, 2019), the M 7.1 rupture appears to be geometrically simpler at depth than near the surface, where it branches out into splay faults of variable dip and strike. Accurately located aftershocks indicate a fairly linear rupture that strikes ~320° (Fig. 4a), with a gentle "helix-like" rotation from the westward dip in the north, to the eastward dip in the south (Fig. 4b). In contrast, geodetically and geologically mapped fault trace exhibits deviations from the main trend illuminated by aftershocks, both along strike and down-dip. In particular, the fault trace is shifted to the west with respect to the aftershock cloud in the central part of the rupture (Fig. 4a), where the largest slip is inferred from the inversion (Figs. 9 and 10). The shift is larger than that estimated by projecting the steeply dipping aftershock lineations to the surface. We interpret these observations as indicating a "Y-shaped" rupture geometry in the top few kilometers of the crust (Fig. 4b), such that the main fault strand splits into two (or more) splay faults with variable dip angles above the depth of 3–4 km. A similar structure is also present to the north of the epicenter, where the two conjugate faults dipping toward each other form a minigraben, with subsidence in between the faults, (see Fig. 7a, around (−15, 35) km in local coordinates), which requires a dip-slip component on the shallow splay faults (Figs. 9 and 10). We refer to this preferred model as "model A." We point out that the rather detailed inferences about the subsurface fault geometry result from a joint analysis of precise seismic, geodetic, and geologic data, and would not be possible from consideration of individual data sets. For example, the aftershock data alone would be insufficient to reveal the details of the rupture geometry in the uppermost crust, which is largely aseismic, and the geodetic and geologic data alone would be insufficient to detect changes in the fault dip angle with depth (Fig. 4). For the sake of completeness, we also considered an alternative fault geometry in which the central part of the earthquake rupture consists of two subparallel subvertical nonintersecting faults. The respective model (model B) is presented in Figures S10 and S11. Although a subvertical western branch results in a somewhat better fit to the data on the western side of the fault, it would imply that the respective rupture segment is essentially devoid of aftershocks throughout the seismogenic layer, which we deem unlikely.

STRESS CHANGES DUE TO THE M 6.4 FORESHOCK AND POSSIBLE TRIGGERING OF THE M 7.1 MAINSHOCK

A close spatiotemporal correlation between the M 6.4 foreshock and the mainshock is suggestive of a cause and effect relationship, and raises a question about possible triggering mechanisms. A number of models were considered to explain interaction between earthquakes, including static (King *et al.*, 1994; Caskey and Wesnousky, 1997; Hardebeck *et al.*, 1998; Anderson and Johnson, 1999; Ziv and Rubin, 2000) and quasistatic (Segall, 1989; Deng and Sykes, 1997; Pollitz and Sacks, 2002; Jonsson *et al.*, 2003) stress transfer, triggering by dynamic stress changes (Lomnitz, 1996; Gomberg *et al.*, 1997; Bellardinelli *et al.*, 1999; Felzer *et al.*, 2002; Tymofyeyeva *et al.*, 2019), and so forth. The 2019 Ridgecrest sequence offers a great opportunity to test the proposed models, not only because it was exceptionally well recorded, but also because it has a history of perturbations by nearby seismic events in which only the most recent perturbation(s) of July 2019 culminated in a major earthquake.

Although our finite-fault model corresponds to a combination of the M 6.4 foreshock and the mainshock, a good agreement between the geodetic moments computed for the left- and right-lateral faults, on the one hand, with the seismic moments of the foreshock and the mainshock, on the other hand, suggests that the seismic moment release due to the M 6.4 foreshock was dominated by slip on the left-lateral northeast-striking faults (segments 6 and 7 in Fig. 4a). This, in turn, suggests that the foreshock involved relatively minor coseismic slip on a right-lateral northwest-trending fault revealed by the aftershock activity following the M 6.4 event (Ross *et al.*, 2019; Chen *et al.*, 2020). We verify this inference by comparing surface displacements due to the left-lateral faults from our best-fitting slip model to the GNSS observations of coseismic offsets due to the M 6.4 event (Floyd *et al.*, 2020). Figure S12 shows the model predictions (red arrows) and the observed horizontal displacements (blue arrows) from the cGNSS (white dots) and campaign (yellow triangles) GNSS sites. The data and the model predictions are in general agreement, including the high-fidelity cGNSS data. The fit to the campaign GNSS data is surprisingly good, considering that some of the sites have not been surveyed up to ~20 yr prior to the 2019 earthquakes. Although these results confirm that the moment release due to the M 6.4 foreshock was dominated by slip on the left-lateral faults (approximated by segments 6 and 7 in our coseismic model, see Fig. 4a), subsequently we show that some amount of slip on the right-lateral northwest-striking rupture is required to produce positive static Coulomb stress changes at the hypocenter of the M 7.1 mainshock.

We ran several tests to see how much slip could have occurred on a right-lateral fault during the M 6.4 foreshock. The model starts to notably overpredict the GNSS data, if the magnitude of an equivalent event on a right-lateral fault exceeds 5.8 (which corresponds to ~0.4 m of average slip on a northwest-striking fault segment). Figure 11 shows the observed and modeled horizontal displacements due to the M 6.4 foreshock involving slip on a system of high-angle antithetic strike-slip faults (denoted by green lines in Fig. 11). We note that M 5.8 is an upper bound on the equivalent amount of slip on the right-lateral fault. A larger moment release on the respective rupture segment would result in an overprediction of both the surface displacements measured by the GNSS and the scalar seismic moment (M 6.4, see Data and Resources).

We used finite-fault models derived for the M 6.4 event to compute static stress changes at the hypocenter of the M 7.1 mainshock. An important parameter in estimation of the induced stress changes is the orientation of a receiver fault. This is particularly relevant for the M 7.1 Ridgecrest event, given its complicated rupture geometry. In previous studies (e.g., Barnhart *et al.*, 2019), static stress changes at the hypocenter of the 5 July mainshock were computed, assuming that the earthquake rupture at depth follows the strike of the fault trace at the Earth surface. However, a comparison of the geometry of precisely relocated aftershocks and the fault trace show that the two are not necessarily correlated, as discussed in the Joint Inversions of Surface Displacement Data section. Therefore, we performed calculations for a range of possible fault orientations (see Data and Resources). Unless noted otherwise, all stress calculations presented later were performed using layered elastic half-space models, assuming a rigidity structure shown in Figure 5. Figure 12a–c show stress perturbations due to slip on the left-lateral fault segments 6 and 7 (see Figs. 4 and 11) resolved on vertical planes striking 320°, coincident with the overall trend of aftershocks of the M 7.1 rupture (Fig. 4). Stresses were computed at the hypocenter depth of the M 7.1 event. Estimates of the hypocenter depth vary between 2 and 8 km below the mean sea level, depending on a method used (Hauksson and Jones, 2020). In our calculations, we assume the depth of 7 km, accounting for the local elevation, and close to the values suggested by the full-waveform inversions, as most reliable (Hauksson and Jones, 2020). Numerical tests show that the computed stress changes are not strongly dependent on the assumed depth of the hypocenter of the M 7.1 event.

As one can see from Figure 12a–c, both shear and normal stress changes caused by slip on the left-lateral faults involved in the M 6.4 foreshock at the hypocenter of the M 7.1 rupture are close to zero, assuming that the mainshock nucleated on a slip plane aligned with the general trend of the M 7.1 rupture (Fig. 4). The computed Coulomb stress change is negligible compared with the negative Coulomb stress change due to a pair of M 5+ earthquakes that occurred in 1995 (Hauksson *et al.*, 1995) in the immediate vicinity of the hypocenter of the 2019 M 7.1 event (Fig. 12d–f, also see Figs. S15 and S16). A more northerly fault strike of 340°, consistent with a focal mechanism derived from the *P*-wave arrivals (see Data and Resources),

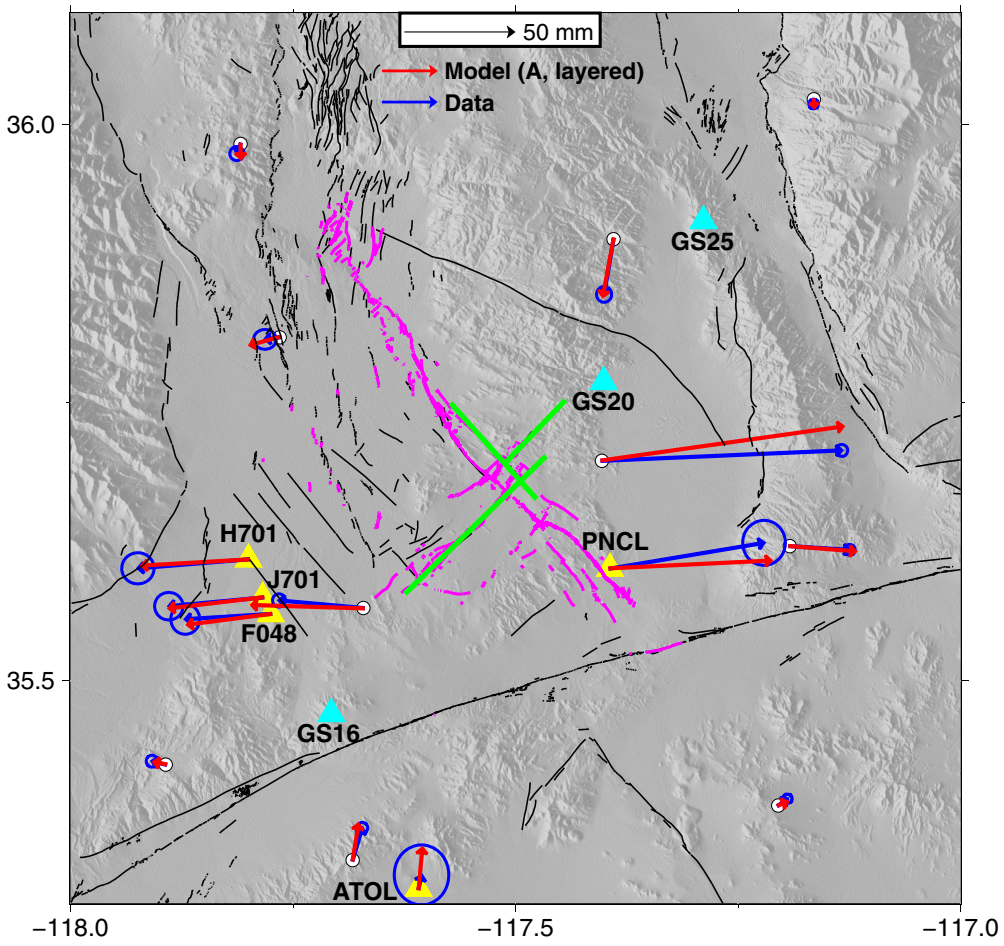

Figure 11. Observed (blue arrows) and modeled (red arrows) horizontal coseismic displacements due to the M 6.4 foreshock. White circles denote the continuous and yellow triangles denote the campaign GNSS sites. Data are from Floyd *et al.* (2020). The ellipses show the 2σ errors. Green lines denote the modeled faults, including the left-lateral southwest-trending fault segments 6, 7, and the right-lateral northwest-trending fault segment 4 (see Fig. 4a). Magenta lines represent surface traces of the 2019 earthquakes (Ponti *et al.*, 2020), and black lines represent Quaternary faults (Jennings and Bryant, 2010). The color version of this figure is available only in the electronic edition.

provides for a more favorable orientation (Fig. 12i), but the resolved Coulomb stress is still negative or close to zero. These calculations show that slip on the left-lateral faults that dominated the moment release from the M 6.4 foreshock had a nearly neutral effect on the nucleation of the mainshock and was certainly insufficient to overcome the stress shadow cast by the 1995 events. Allowing for a right-lateral slip on the northwest-striking fault with an equivalent moment magnitude of 5.8 results in the positive Coulomb stress changes at the mainshock hypocenter (Fig. 12l). Our calculations indicate that if the M 7.1 event was triggered by static stress transfer due to foreshocks, the triggering was due to slip on the same right-lateral fault that was subsequently ruptured by the mainshock.

We also investigated the role of the second largest foreshock, the M 5.4 event that occurred just hours before and a few kilometers away from the hypocenter of the mainshock. An earlier study by Barnhart *et al.* (2019) assumed that the M 5.4 event occurred on a northwest-trending right-lateral fault and estimated a positive Coulomb stress change of ~70 kPa at the hypocenter of the M 7.1 event. However, detailed seismic studies showed that the M 5.4 aftershock occurred on a left-lateral northeast-trending fault (e.g., Shelly, 2020). Given a relatively small size of the foreshock, we generated a finite-fault model, assuming a circular rupture with a Gaussian slip distribution, subject to a constraint that the geodetic moment equals the seismic moment. The rupture centroid and the effective radius were chosen such that most of the precisely located aftershocks of the M 5.4 event occur on a periphery of the assumed slip distribution, as expected from the stress concentration arguments (e.g., Fialko, 2015). The calculated Coulomb stress changes at the mainshock hypocenter were found to be negative. However, sensitivity tests showed that the results are quite dependent on the assumed position of the centroid of the M 5.4 rupture, because of its close proximity to the mainshock hypocenter. In particular, perturbing the along-strike centroid location by 2 km (likely within the uncertainties of the assumed slip distribution) affects the sign of the cumulative Coulomb stress change due to the 1995–2019 premainshock sequence (Fig. 13). Thus, the answer to the question "was the nucleation of the M 7.1 mainshock advanced by the cumulative static stress changes due to the nearby earthquakes" depends on details of slip models of the respective earthquakes, most notably the 2019 M 5.4 foreshock, that are not well constrained by the available data. For values of the effective coefficient of friction that are higher than that assumed in calculations presented in this study (0.4), the predicted Coulomb stress changes are more negative, as the normal stress changes at the mainshock hypocenter are predominantly compressive (Fig. 13b,e).

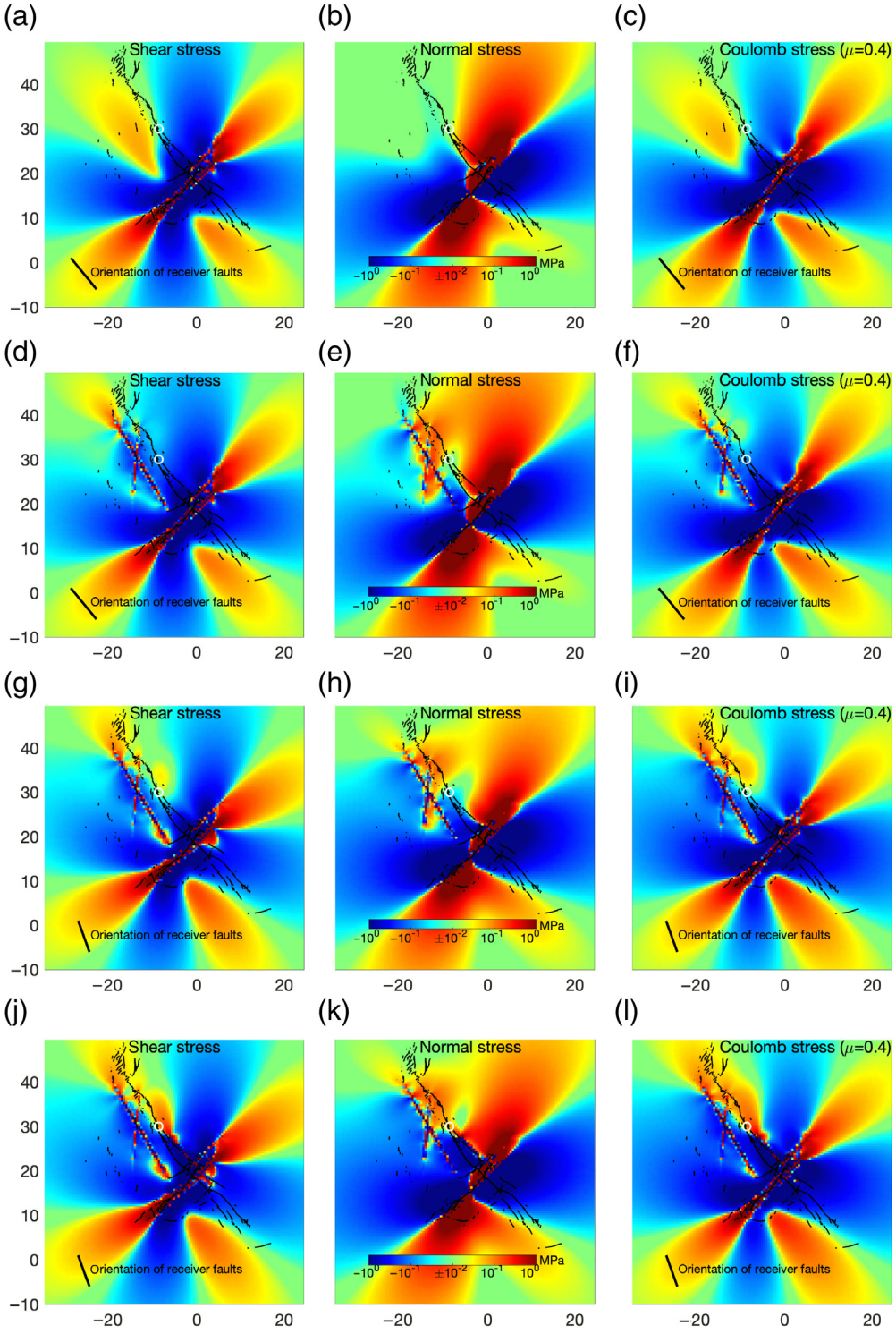

Figure 12. Static stress changes due to the premainshock seismicity. Stress changes are computed at depth of 7 km. (a–c) Receiver faults striking 320° (average strike of the M 7.1 mainshock). (d–f) Same as (a–c), plus stress changes from a pair of 1995 M 5+ events. (g–i) Same as (d–f), for receiver faults striking 340° (consistent with the focal mechanism based on the first-motion data). (j–l) Same as (g–i), but including the northwest-striking segment (see Fig. 11). The Coulomb stress change was calculated assuming the coefficient of friction of 0.4. White circle denotes the epicenter of the M 7.1 mainshock. Orientation of receiver faults is shown by a black solid line. Black wavy line denotes the rupture trace. The color version of this figure is available only in the electronic edition.

It is interesting to note that the hypocenter of the 2019 M 7.1 event has experienced positive Coulomb stress changes due to shaking from the nearby events that were considerably (up to an order of magnitude) higher than the estimated static stress changes (see Fig. S17), yet the former failed to trigger a major earthquake at the time of shaking. This is evidence for the importance of quasistatic nucleation, rather than a critical yield stress, as the condition for triggering. Based on the results presented in this section, we conclude that the 2019 M 7.1 mainshock nucleated on a fault oriented 340° (20° west of north) that was likely nudged toward failure by the M 6.4 foreshock, and subsequently either encouraged or discouraged by the M 5.4 foreshock. Upon nucleating, the rupture propagated along a system of pre-existing faults on average striking 320° (40° west of north). Activation of the pre-existing faults that were presumably less optimally oriented for failure with respect to the local stress field compared with the nucleation site could result from the onset of dynamic weakening (e.g., Rice, 2006; Reches and Lockner, 2010; Di Toro *et al.*, 2011; Brown and Fialko, 2012).

DISCUSSION

The 2019 M 7.1 Ridgecrest earthquake shares a lot of similarities with the previous major earthquake that occurred in the ECSZ, the 1999 Hector Mine event (Fig. 14). Both events nucleated on a fault strand striking at a larger angle compared with the average strike of the whole rupture. In case of the Hector Mine event, the

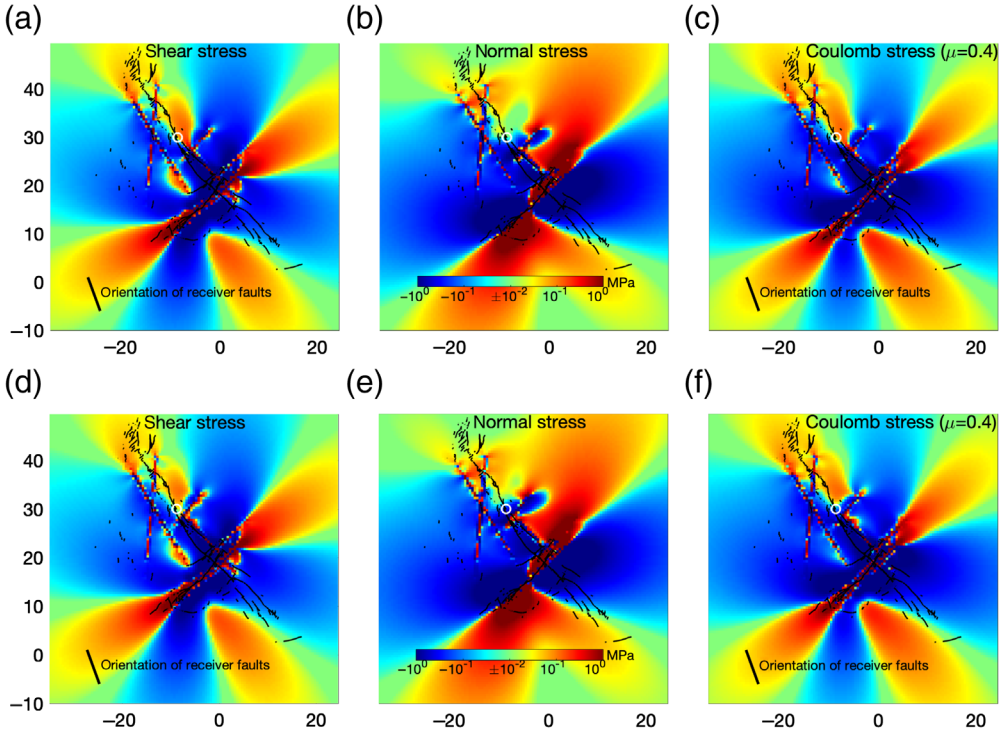

Figure 13. Same as in Figure 12, but including the 2019 M 5.4 foreshock. The receiver fault strike is 340°. (a–c) The M 5.4 event translated 2 km in southeast direction with respect to the estimated moment centroid. (d–f) The M 5.4 event translated 2 km in northwest direction with respect to the estimated moment centroid. The color version of this figure is available only in the electronic edition.

fault strike correlates with topography (Fialko, Rivera, and Kanamori, 2005); however, no such correlation exists in case of the Ridgecrest event, so that stresses due to topography cannot explain different orientations of the nucleation sites. A more likely explanation is that both earthquakes nucleated on a local structure that was more favorably oriented with respect to the regional stress field and proceeded to rupture pre-existing faults that have been rotated away from an optimal orientation over time (e.g., by simple shear). If so, the rupture process may have involved dynamic triggering and weakening of the pre-existing faults.

Both the Ridgecrest and the Hector Mine ruptures exemplify complexity of immature developing strike-slip fault zones, with multiple subparallel branches and along-strike variations in the dip angle. Coseismic slip on closely spaced subparallel fault strands is puzzling, as dynamic rupture on a given fault interface is expected to discourage slip on nearby potential slip interfaces. More sophisticated dynamic rupture models are needed to better understand observations of slip on multiple subparallel fault strands. Finally, for both the Ridgecrest and the Hector Mine events, some of the fault strands broke the surface, whereas other strands remained blind and could only be detected with the help of precisely located aftershocks.

Among the main differences between the two events are the abundant cross faults and shallow splay faults in case of the Ridgecrest earthquake. In part, this difference could be attributed to regional variations in the stress regime. The Ridgecrest earthquakes occurred in a transtensional domain with concurrent strike-slip and normal faulting, as evidenced by, for example, the 1995 earthquake sequence that involved a pair of closely spaced strike-slip and normal faults (Hauksson *et al.*, 1995, also, see Figs. S13 and S14). The shallow splay faults inferred from our inversions have dip angles around 60°–70°, close to optimal orientation for normal faults. We interpret them as normal faults activated to accommodate a combination of the right-lateral slip and extension across the ECSZ. The geometry of our best-fit models in the shallow crust closely resembles the so-called "flower structures" recognized on a number of strike-slip faults worldwide (Harding, 1985; Sylvester, 1988; Bayasgalan *et al.*, 1999).

It is of interest to evaluate how the coseismic slip amplitude varies with depth. Previous studies have suggested that for a number of M ∼ 7 strike-slip earthquakes the amount of slip in the middle of the seismogenic layer systematically exceeds the amount of slip at the surface (Fialko, Sandwell, *et al.*, 2005; Wang *et al.*, 2014; Hussain *et al.*, 2016). Although such behavior would be entirely expected for faults cutting through the velocity-strengthening layer in the top few kilometers of the Earth's crust (Marone and Scholz, 1988; Hudnut and Sieh, 1989; Johnson *et al.*, 2006), where the coseismic slip is inhibited and most of slip occurs aseismically, for many faults that exhibit a larger coseismic slip at depth there is no evidence that aseismic slip is present and/or sufficiently robust to balance the slip budget. Such behavior, known as the shallow slip deficit (SSD), could be attributed to a number of mechanisms, including the presence of a soft damage zone (Barbot, Fialko, and Sandwell, 2008) and dynamic damage due to propagating rupture fronts (Kaneko and Fialko, 2011; Roten *et al.*, 2017). Inversions of high-quality geodetic data also show that a number of large strike-slip (or mixed mode) earthquakes are not associated with the SSD, although such events tend to be on

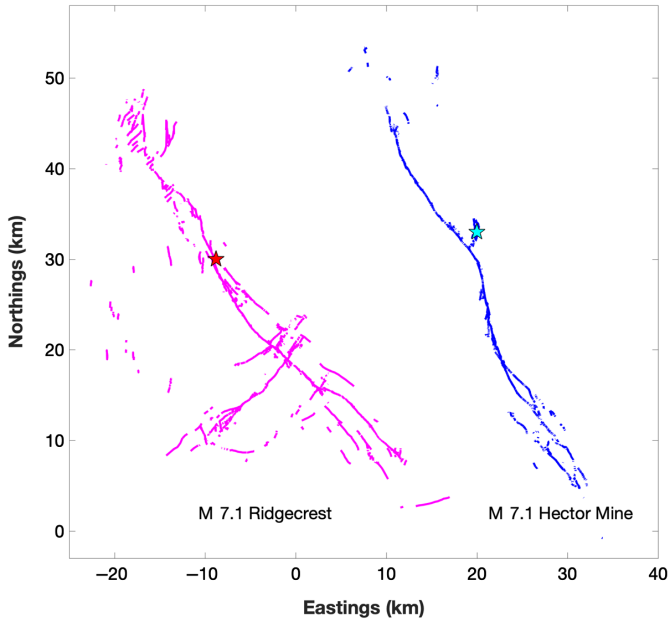

Figure 14. A comparison of the 2019 Ridgecrest and the 1999 Hector Mine rupture traces. The color version of this figure is available only in the electronic edition.

a high end of the M 7–8 range (e.g., Tong *et al.*, 2010; Zinke *et al.*, 2014), possibly indicating differences between rupture styles on mature and immature faults.

Figure 15a shows a normalized distribution of slip as a function of depth for the M 7.1 Ridgecrest earthquake (black solid line) obtained from our best-fitting model for a layered half-space (Fig. 10), as well as for a number of other strike-slip earthquakes of comparable size for which high-quality geodetic data are available (color dashed lines). As one can see from Figure 15a, the maximum average slip due to the mainshock of the Ridgecrest sequence occurred in the depth interval between 3 and 4 km, essentially the same as inferred for other major strike-slip earthquakes analyzed using a consistent methodology. The estimated amount of the SSD is on the order of 30%, although the amplitude obviously depends on the degree of smoothing, with greater smoothing resulting in smaller variations in the slip amplitude with depth. It is interesting to note that the inferred peak in the seismic moment release for system-size earthquakes that rupture the entire seismogenic layer (Fig. 15a) is also apparent in the depth distribution of small earthquakes. Figure 15b shows the depth distribution of all of seismicity in California, as well as the aftershocks of the 2019 Ridgecrest earthquakes (see Data and Resources). We culled the earthquake catalogs to exclude events that have an absolute depth error greater than 1 km and assigned the data to 1 km depth bins. The resulting data set consisting of $\sim 10^6$ events has a maximum in the mid-upper seismogenic zone, approximately in the same depth interval as the peak in the coseismic moment release by large earthquakes (Fig. 15a). This is in contrast with models that predict that the most favorable conditions for the earthquake occurrence are met at the bottom of the seismogenic zone (Sibson, 1982; Jiang and Fialko, 2016; Jiang and Lapusta, 2016). Given the average thickness of the seismogenic layer in the continental crust on the order of 12–14 km (e.g., Wright *et al.*, 2013), results shown in Figure 15 suggest that the depth interval most conducive to unstable slip is in the upper part of the seismogenic zone. Catalogs of precisely located earthquakes with low magnitude of completeness from other seismically active regions are needed to test whether a similar depth dependence of "seismogenic potential" exists elsewhere.

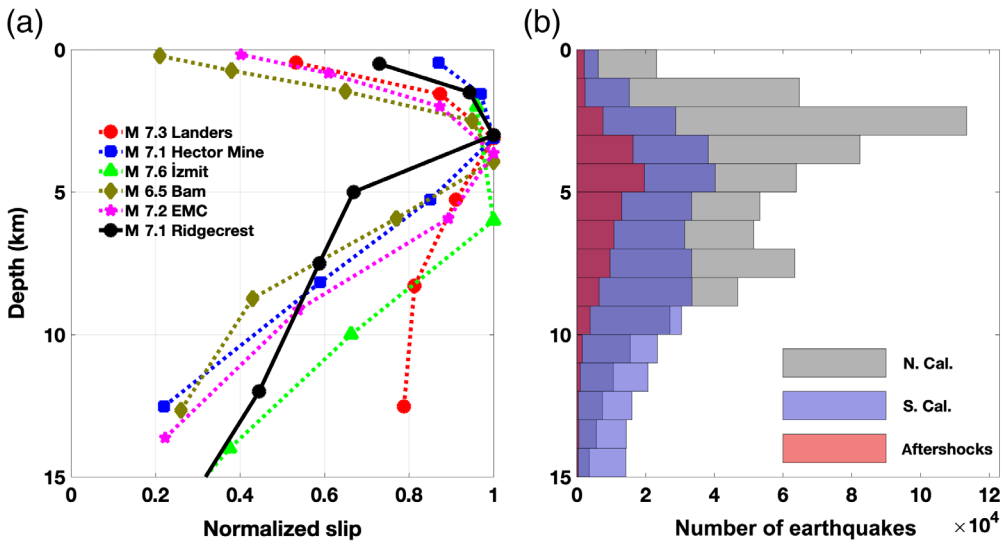

Figure 15. (a) Along-strike averaged coseismic slip as a function of depth for the 5 July M 7.1 Ridgecrest earthquake (black solid line), as well as for several other M ∼ 7 strike-slip earthquakes (color dashed lines, data from Fialko, Sandwell, *et al.*, 2005; Kaneko and Fialko, 2011). (b) Depth distribution of seismicity in California (see Data and Resources), and aftershocks of the 2019 Ridgecrest sequence (Ross *et al.*, 2019). The magnitude completeness of the respective earthquake catalogs is 1–1.5. EMC, El Mayor–Cucapah earthquake. The color version of this figure is available only in the electronic edition.

CONCLUSIONS

The 5 July 2019 M 7.1 Ridgecrest earthquake was the largest earthquake in southern California since the 1999 Hector Mine earthquake, with which it shared a number of similarities. The Ridgecrest

earthquake is characterized by a complex rupture geometry involving subparallel fault strands, along-strike variations in the dip angle, and shallow variations in the fault strike. The maximum slip occurred on shallow splay faults that were likely reactivated normal faults forming a classic "flower structure" on top of a reasonably straight right-lateral strike-slip fault at depth. Nucleation of unstable slip at the hypocenter of the M 7.1 mainshock was discouraged by the pair of the M 5+ events that occurred in the immediate vicinity of the hypocenter in August–September of 1995, only weakly if at all affected by slip on a left-lateral branch of the M 6.4 foreshock, encouraged by slip on a right-lateral branch of the M 6.4 foreshock, and likely discouraged by the M 5.4 foreshock that occurred hours before the mainshock. Static stress changes near the hypocenter resolved on a mean trend of the M 7.1 rupture were less favorable for failure compared with stress changes resolved on a more northerly striking fault plane indicated by the first-motion data. This suggests that the M 7.1 mainshock may have been triggered by the M 6.4 foreshock on a slip patch that was optimally oriented for failure with respect to the local stress field, and subsequently triggered unstable slip on a less favorably oriented preexisting right-lateral fault system. Dynamic stress changes from the nearby earthquakes failed to trigger the mainshock, despite the fact that they were much larger than any static stress change that might have advanced the nucleation of unstable slip. Slip models derived from inversions of surface deformation data reveal a moderate amount of SSD. Subsequent studies of postseismic deformation will show if the inferred amount of the coseismic slip deficit can be accommodated by means of creep in the uppermost crust. The estimated depth of the maximum slip averaged along the rupture length is 3–4 km, similar to results from previous studies of major strike-slip earthquakes and to the depth distribution of precisely located seismicity in California, suggesting that the respective depth interval maximizes a potential for seismic instabilities.

DATA AND RESOURCES

First-motion focal mechanism of the 2019 M 7.1 mainshock is available at https://earthquake.usgs.gov/earthquakes/eventpage/ci38457511/focal-mechanism (last accessed November 2019). Seismic moment of the 2019 M 7.1 mainshock is available at https://earthquake.usgs.gov/earthquakes/eventpage/ci38457511/moment-tensor (last accessed November 2019). Seismic moment of the 2019 M 6.4 foreshock is available at https://earthquake.usgs.gov/earthquakes/eventpage/ci38443183/moment-tensor (last accessed November 2019). Seismic moment of the 2019 M 5.4 foreshock is available at https://earthquake.usgs.gov/earthquakes/eventpage/ci38450263/moment-tensor (last accessed November 2019). We have used parametric data and focal mechanisms from the California Institute of Technology (Caltech)/U.S. Geological Survey (USGS) Southern California Seismic Network (SCSN), doi: 10.7914/SN/CI; stored at the Southern California Earthquake Data Center (SCEDC), doi: 10.7909/C3WD3xH1. Waveform relocated earthquake catalog for southern California is available at https://scedc.caltech.edu/research-tools/alt-2011-yang-hauksson-shearer.html (last accessed November 2019). Double-difference relocated earthquake catalog for northern California is provided by the Northern California Earthquake Data Center (NCEDC), doi: 10.7932/NCEDC, available online at https://www.ncedc.org/ncedc/catalog-search.html (last accessed November 2019). Movies of stress changes due to the largest foreshocks of the 2019 sequence and the 1995 earthquakes, spanning all possible fault strikes, are available at https://igppweb.ucsd.edu/~fialko/ridgecrest.html (last accessed May 2020). The supplemental material contains additional text and Figures S1–S17 to support the main article.

ACKNOWLEDGMENTS

The authors thank the two anonymous reviewers and Editor Timothy Dawson for thorough and insightful reviews. This study was supported by National Aeronautics and Space Administration (NASA; Grant 80NSSC18K0466) and National Science Foundation (NSF; Grants EAR-1841273 and EAR-1945760). Sentinel-1 data were provided by the European Space Agency (ESA) through Alaska Satellite Facility (ASF) and UNAVCO. Digital elevation data were provided by NASA and German Aerospace Center (DLR). Some of the figures were generated using the Generic Mapping Tools (GMT) (Wessel *et al.*, 2013), and the MATLAB is available at https://www.mathworks.com/products/matlab.html (last accessed April 2020).

REFERENCES

Ahmed, R., P. Siqueira, S. Hensley, B. Chapman, and K. Bergen (2011). A survey of temporal decorrelation from spaceborne L-Band repeat-pass InSAR, *Remote Sens. Environ.* **115,** 2887–2896.

Anderson, G., and H. Johnson (1999). A new statistical test for static stress triggering: Application to the 1987 Superstition Hills earthquake sequence, *J. Geophys. Res.* **104,** 20,153–20,168.

Barbot, S., Y. Fialko, and Y. Bock (2009). Postseismic deformation due to the M_w 6.0 2004 Parkfield earthquake: Stress-driven creep on a fault with spatially variable rate-and-state friction parameters, *J. Geophys. Res.* **114,** no. B07405, doi: 10.1029/2008JB005748.

Barbot, S., Y. Fialko, and D. Sandwell (2008). Effect of a compliant fault zone on the inferred earthquake slip distribution, *J. Geophys. Res.* **113,** no. B06404, doi: 10.1029/2007JB005256.

Barbot, S., Y. Fialko, and D. Sandwell (2009). Three-dimensional models of elasto-static deformation in heterogeneous media, with applications to the Eastern California Shear Zone, *Geophys. J. Int.* **179,** 500–520.

Barbot, S., Y. Hamiel, and Y. Fialko (2008). Space geodetic investigation of the co- and post-seismic deformation due to the 2003 M_w 7.1 Altai earthquake: Implications for the local lithospheric rheology, *J. Geophys. Res.* **113,** no. B03403, doi: 10.1029/2007JB005063.

Barnhart, W. D., G. P. Hayes, and R. D. Gold (2019). The July 2019 Ridgecrest, California, earthquake sequence: Kinematics of slip and stressing in cross-fault ruptures, *Geophys. Res. Lett.* **46,** 11,859–11,867.

Bayasgalan, A., J. Jackson, J.-F. Ritz, and S. Carretier (1999). Forebergs', flower structures, and the development of large intra-continental strike-slip faults: The Gurvan Bogd fault system in Mongolia, *J. Struct. Geol.* **21,** 1285–1302.

Bellardinelli, M. E., M. Cocco, O. Coutant, and F. Cotton (1999). Redistribution of dynamic stress during coseismic ruptures: Evidence for fault interaction and earthquake triggering, *J. Geophys. Res.* **104,** 14,925–14,945.

Bishop, C. M. (1995). Training with noise is equivalent to Tikhonov regularization, *Neural Comput.* **7,** 108–116.

Brown, K. M., and Y. Fialko (2012). "Melt welt" mechanism of extreme weakening of gabbro at seismic slip rates, *Nature* **488,** 638–641.

Caskey, S. J., and S. G. Wesnousky (1997). Static stress change and earthquake triggering during the 1954 Fairview Peak and Dixie Valley earthquakes, Central Nevada, *Bull. Seismol. Soc. Am.* **87,** 521–527.

Chen, K., J.-P. Avouac, S. Aati, C. Milliner, F. Zheng, and C. Shi (2020). Cascading and pulse-like ruptures during the 2019 Ridgecrest earthquakes in the Eastern California Shear Zone, *Nat. Comm.* **11,** 1–8.

Deng, J., and L. R. Sykes (1997). Evolution of the stress field in Southern California and triggering of moderate-size earthquakes: A 200-year perspective, *J. Geophys. Res.* **102,** 9859–9886.

Di Toro, G., R. Han, T. Hirose, N. De Paola, S. Nielsen, K. Mizoguchi, F. Ferri, M. Cocco, and T. Shimamoto (2011). Fault lubrication during earthquakes, *Nature* **471,** 494–498.

Dokka, R. K., and C. J. Travis (1990). Role of the Eastern California shear zone in accommodating Pacific-North American plate motion, *Geophys. Res. Lett.* **17,** 1323–1327.

Farr, T., and M. Kobrick (2000). Shuttle Radar Topography Mission produces a wealth of data, *Eos Trans. AGU* **81,** 583–585.

Felzer, K. R., T. W. Becker, R. E. Abercrombie, G. Ekström, and J. R. Rice (2002). Triggering of the 1999 Mw 7.1 Hector Mine earthquake by aftershocks of the 1992 Mw 7.3 Landers earthquake, *J. Geophys. Res.* **107,** ESE-6.

Fialko, Y. (2004). Probing the mechanical properties of seismically active crust with space geodesy: Study of the co-seismic deformation due to the 1992 M_w 7.3 Landers (southern California) earthquake, *J. Geophys. Res.* **109,** no. B03307, doi: 10.1029/2003JB002756.

Fialko, Y. (2015). Fracture and frictional mechanics—Theory, in *Treatise on Geophysics*, G. Schubert (Editor), Second Ed., Vol. 4, Elsevier Ltd., Oxford, United Kingdom, 73–91.

Fialko, Y., Z. Jin, E. Tymofyeyeva, and M. A. Floyd (2019). Ridgecrest California earthquake post-event response July 2019 UCSD, *Technical Report*, UNAVCO, Inc., GPS/GNSS Observations Dataset, doi: 10.7283/YJK0-B215.

Fialko, Y., Z. Jin, E. Tymofyeyeva, D. T. Sandwell, J. Haase, and M. A. Floyd (2019). Ridgecrest California earthquake response July 2019 UCSD, *Technical Report*, UNAVCO, Inc., GPS/GNSS Observations Dataset, doi: 10.7283/N74Q-GA66.

Fialko, Y., L. Rivera, and H. Kanamori (2005). Estimate of differential stress in the upper crust from variations in topography and strike along the San Andreas fault, *Geophys. J. Int.* **160,** 527–532.

Fialko, Y., D. Sandwell, M. Simons, and P. Rosen (2005). Three-dimensional deformation caused by the Bam, Iran, earthquake and the origin of shallow slip deficit, *Nature* **435,** 295–299.

Fialko, Y., M. Simons, and D. Agnew (2001). The complete (3-D) surface displacement field in the epicentral area of the 1999 M_w 7.1 Hector Mine earthquake, southern California, from space geodetic observations, *Geophys. Res. Lett.* **28,** 3063–3066.

Floyd, M., G. Funning, Y. A. Fialko, R. L. Terry, and T. Herring (2020). Survey and continuous GNSS in the vicinity of the July 2019 Ridgecrest earthquakes, *Seismol. Res. Lett.* doi: 10.1785/0220190324.

Goldstein, R. M., H. A. Zebker, and C. L. Werner (1988). Satellite radar interferometry: Two-dimensional phase unwrapping, *Radio Sci.* **23,** 713–720.

Golub, G. H., P. C. Hansen, and D. P. O'Leary (1999). Tikhonov regularization and total least squares, *SIAM J. Matrix Anal. Appl.* **21,** 185–194.

Gomberg, J., M. L. Blanpied, and N. M. Beeler (1997). Transient triggering of near and distant earthquakes, *Bull. Seismol. Soc. Am.* **87,** 294–309.

Gonzalez-Ortega, A., Y. Fialko, D. Sandwell, F. Alejandro Nava-Pichardo, J. Fletcher, J. Gonzalez-Garcia, B. Lipovsky, M. Floyd, and G. Funning (2014). El Mayor-Cucapah (M_w 7.2) earthquake: Early near-field postseismic deformation from InSAR and GPS observations, *J. Geophys. Res.* **119,** 1482–1497.

Hardebeck, J. L., J. J. Nazareth, and E. Hauksson (1998). The static stress change triggering model: Constraints from two southern California aftershock sequences, *J. Geophys. Res.* **103,** 24,427–24,437.

Harding, T. P. (1985). Seismic characteristics and identification of negative flower structures, positive flower structures, and positive structural inversion, *AAPG Bulletin* **69,** 582–600.

Hauksson, E., and L. Jones (2020). Seismicity, stress state, and style of faulting of the Ridgecrest-Coso region from the 1930s through 2019: Seismotectonics of an evolving plate boundary segment, *Bull. Seismol. Soc. Am.* doi: 10.1785/0120200051.

Hauksson, E., and J. Unruh (2007). Regional tectonics of the Coso geothermal area along the intracontinental plate boundary in central eastern California: Three-dimensional V_p and V_p/V_s and models, spatial-temporal seismicity patterns, and seismogenic deformation, *J. Geophys. Res.* **112,** no. B06309, doi: 10.1029/2006JB004721.

Hauksson, E., K. Hutton, H. Kanamori, L. Jones, J. Mori, S. Hough, and G. Roquemore (1995). Preliminary report on the 1995 Ridgecrest earthquake sequence in eastern California, *Seismol. Res. Lett.* **66,** 54–60.

Hauksson, E., L. Jones, and K. Hutton (2002). The 1999 M_w 7.1 Hector Mine, California, earthquake sequence: Complex conjugate strike-slip faulting, *Bull. Seismol. Soc. Am.* **92,** 1154–1170.

Hauksson, E., P. Small, K. Hafner, R. Busby, R. Clayton, J. Goltz, T. Heaton, K. Hutton, H. Kanamori, J. Polet, *et al.* (2001). Southern California seismic network: Caltech/USGS element of TriNet 1997-2001, *Seismol. Res. Lett.* **72,** 690–704.

Herring, T. A., T. I. Melbourne, M. H. Murray, M. A. Floyd, W. M. Szeliga, R. W. King, D. A. Phillips, C. M. Puskas, M. Santillan, and L. Wang (2016). Plate Boundary Observatory and related networks: GPS data analysis methods and geodetic products, *Rev. Geophys.* **54,** 759–808.

Hudnut, K. W., and K. E. Sieh (1989). Behavior of the Superstition Hills fault during the past 330 years, *Bull. Seismol. Soc. Am.* **79,** 304–329.

Hussain, E., T. J. Wright, R. J. Walters, D. Bekaert, A. Hooper, and G. A. Houseman (2016). Geodetic observations of postseismic creep in the decade after the 1999 Izmit earthquake, Turkey: Implications for a shallow slip deficit, *J. Geophys. Res.* **121,** 2980–3001.

Jennings, C., and W. Bryant (2010). Fault activity map of California, *California Division of Mines and Geology, Geologic Data Map No. 6*, 1:750,000.

Jiang, J., and Y. Fialko (2016). Reconciling seismicity and geodetic locking depths on the Anza section of the San Jacinto fault, *Geophys. Res. Lett.* **43,** 10,663–10,671.

Jiang, J., and N. Lapusta (2016). Deeper penetration of large earthquakes on seismically quiescent faults, *Science* **352,** 1293–1297.

Johnson, K. M., R. Bürgmann, and K. Larson (2006). Frictional properties on the San Andreas fault near Parkfield, California, inferred from models of afterslip following the 2004 earthquake, *Bull. Seismol. Soc. Am.* **96,** S321–S338.

Jonsson, S., P. Segall, R. Pedersen, and G. Bjornsson (2003). Post-earthquake ground movements correlated to pore-pressure transients, *Nature* **424,** 179–183.

Jonsson, S., H. Zebker, P. Segall, and F. Amelung (2002). Fault slip distribution of the 1999 M_w 7.1 Hector Mine, California, earthquake, estimated from satellite radar and GPS measurements, *Bull. Seismol. Soc. Am.* **92,** 1377–1389.

Kaneko, Y., and Y. Fialko (2011). Shallow slip deficit due to large strike-slip earthquakes in dynamic rupture simulations with elasto-plastic off-fault response, *Geophys. J. Int.* **186,** 1389–1403.

King, G. C. P., R. S. Stein, and J. Lin (1994). Static stress changes and the triggering of earthquakes, *Bull. Seismol. Soc. Am.* **84,** 935–953.

Liu, C., T. Lay, E. E. Brodsky, K. Dascher-Cousineau, and X. Xiong (2019). Coseismic rupture process of the large 2019 Ridgecrest earthquakes from joint inversion of geodetic and seismological observations, *Geophys. Res. Lett.* **46,** 11,820–11,829.

Lomnitz, C. (1996). Search of a worldwide catalog for earthquakes triggered at intermediate distances, *Bull. Seismol. Soc. Am.* **86,** 293–298.

Marone, C., and C. H. Scholz (1988). The depth of seismic faulting and the upper transition from stable to unstable slip regimes, *Geophys. Res. Lett.* **15,** 621–624.

McClusky, S., S. Bjornstad, B. Hager, R. King, B. Meade, M. Miller, F. Monastero, and B. Souter (2001). Present day kinematics of the Eastern California Shear Zone from a geodetically constrained block model, *Geophys. Res. Lett.* **28,** 3369–3372.

Mitchell, E., Y. Fialko, and K. M. Brown (2016). Velocity-weakening behavior of Westerly granite at temperature up to 600° C, *J. Geophys. Res.* **121,** 6932–6946.

Nur, A., H. Ron, and G. Beroza (1993). The nature of the Landers-Mojave earthquake line, *Science* **261,** 201–203.

Okada, Y. (1985). Surface deformations due to shear and tensile faults in a halfspace, *Bull. Seismol. Soc. Am.* **75,** 1135–1154.

Pollitz, F. F., and I. S. Sacks (2002). Stress triggering of the 1999 Hector Mine earthquake by transient deformation following the 1992 Landers earthquake, *Bull. Seismol. Soc. Am.* **92,** 1487–1496.

Ponti, D., J. L. Blair, C. Rosa, K. Thomas, A. Pickering, S. Akciz, S. Angster, J. Avouac, J. Bachhuber, S. Bacon, *et al.* (2020). Documentation of surface fault rupture and ground deformation features produced by the Ridgecrest M 6.4 and M 7.1 earthquake sequence of 4 and 5 July 2019, *Seismol. Res. Lett.* doi: 10.1785/0220190322.

Reches, Z., and D. A. Lockner (2010). Fault weakening and earthquake instability by powder lubrication, *Nature* **467,** 452–455.

Rice, J. R. (2006). Heating and weakening of faults during earthquake slip, *J. Geophys. Res.* **111,** no. B05311, doi: 10.1029/2005JB004006.

Rice, J. R., and S. T. Tse (1986). Dynamic motion of a single degree of freedom system following a rate and state dependent friction law, *J. Geophys. Res.* **91,** 521–530.

Rosen, P. A., S. Hensley, H. A. Zebker, F. H. Webb, and E. J. Fielding (1996). Surface deformation and coherence measurements of Kilauea Volcano, Hawaii, from SIR-C radar interferometry, *J. Geophys. Res.***101 ,** no. E10, 23,109–23,125.

Ross, Z. E., B. Idini, Z. Jia, O. L. Stephenson, M. Zhong, X. Wang, Z. Zhan, M. Simons, E. J. Fielding, S.-H. Yun, *et al.* (2019). Hierarchical interlocked orthogonal faulting in the 2019 Ridgecrest earthquake sequence, *Science* **366,** 346–351.

Roten, D., K. Olsen, and S. Day (2017). Off-fault deformations and shallow slip deficit from dynamic rupture simulations with fault zone plasticity, *Geophys. Res. Lett.* **44,** 7733–7742.

Sandwell, D., R. Mellors, X. Tong, M. Wei, and P. Wessel (2011). Open radar interferometry software for mapping surface deformation, *Eos Trans. AGU* **92,** 234–234.

Sauber, J., W. Thatcher, and S. Solomon (1986). Geodetic measurement of deformation in the central Mojave Desert, California, *J. Geophys. Res.* **91,** 2683–2693.

Segall, P. (1989). Earthquakes triggered by fluid extraction, *Geology* **17,** 942–946.

Shelly, D. R. (2020). A high-resolution seismic catalog for the initial 2019 Ridgecrest earthquake sequence: Foreshocks, aftershocks, and faulting complexity, *Seismol. Res. Lett.* doi: 10.1785/0220190309.

Sibson, R. H. (1982). Fault zone models, heat flow, and the depth distribution of earthquakes in the continental crust of the united states, *Bull. Seismol. Soc. Am.* **72,** 151–163.

Sieh, K., L. Jones, E. Hauksson, K. Hudnut, D. Eberhart-Phillips, T. Heaton, S. Hough, K. Hutton, H. Kanamori, A. Lilje, *et al.* (1993). Near-field investigations of the Landers earthquake sequence, *Science* **260,** 171–176.

Simons, M., Y. Fialko, and L. Rivera (2002). Coseismic deformation from the 1999 M_w 7.1 Hector Mine, California, earthquake, as inferred from InSAR and GPS observations, *Bull. Seismol. Soc. Am.* **92,** 1390–1402.

Sylvester, A. (1988). Strike-slip faults, *Geol. Soc. Am. Bull.* **100,** 1666–1703.

Tong, X., D. Sandwell, and Y. Fialko (2010). Coseismic slip model of the 2008 Wenchuan earthquake derived from joint inversion of interferometric synthetic aperture radar, GPS, and field data, *J. Geophys. Res.* **115,** no. B04314, doi: 10.1029/2009JB006625.

Tymofyeyeva, E., and Y. Fialko (2015). Mitigation of atmospheric phase delays in InSAR data, with application to the eastern California shear zone, *J. Geophys. Res.* **120,** 5952–5963.

Tymofyeyeva, E., Y. Fialko, J. Jiang, X. Xu, D. Sandwell, R. Bilham, T. K. Rockwell, C. Blanton, F. Burkett, A. Gontz, *et al.* (2019). Slow slip event on the southern San Andreas fault triggered by the 2017 M_w 8.2 Chiapas (Mexico) earthquake, *J. Geophys. Res.* **124,** 9956–9975.

Vogel, C. R. (2002). *Computational Methods for Inverse Problems*, Vol. 23, Society for Industrial and Applied Mathematics, Philadelphia, Pennsylvania.

Wang, K., and Y. Fialko (2014). Space geodetic observations and models of postseismic deformation due to the 2005 M7.6 Kashmir (Pakistan) earthquake, *J. Geophys. Res.* **119,** 7306–7318.

Wang, K., and Y. Fialko (2015). Slip model of the 2015 M_w 7.8 Gorkha (Nepal) earthquake from inversions of ALOS-2 and GPS data, *Geophys. Res. Lett.* **42,** 7452–7458.

Wang, K., and Y. Fialko (2018). Observations and modeling of co- and postseismic deformation due to the 2015 M_w 7.8 Gorkha (Nepal) earthquake, *J. Geophys. Res.* **123,** 761–779.

Wang, K., D. Dreger, E. Tinti, R. Bürgrmann, and T. Taira (2020). Rupture process of the 2019 Ridgecrest, California M6.4 foreshock and M7.1 earthquake constrained by seismic and geodetic Data, *Bull. Seismol. Soc. Am.* doi: 10.1785/0120200108.

Wang, K., X. Xu, and Y. Fialko (2017). Improving burst alignment in TOPS interferometry with bivariate enhanced spectral diversity (BESD), *IEEE Geosci. Remote Sens. Lett.* **14,** 2423–2427.

Wang, R., F. Martin, and F. Roth (2003). Computation of deformation induced by earthquakes in a multi-layered elastic crust—FORTRAN programs EDGRN/EDCMP, *Comp. Geosci.* **29,** 195–207.

Wang, Y., Y.-N. N. Lin, M. Simons, and S. T. Tun (2014). Shallow rupture of the 2011 Tarlay earthquake (M_w 6.8), eastern Myanmar, *Bull. Seismol. Soc. Am.* **104,** 2904–2914.

Wessel, P., W. H. F. Smith, R. Scharroo, J. Luis, and F. Wobbe (2013). Generic Mapping Tools: Improved version released, *Eos Trans. AGU* **94,** 409–410.

Wright, T. J., J. R. Elliott, H. Wang, and I. Ryder (2013). Earthquake cycle deformation and the Moho: Implications for the rheology of continental lithosphere, *Tectonophysics* **609,** 504–523.

Zhang, Q., and G. Lin (2014). Three-dimensional V_p and V_p/V_s and models in the Coso geothermal area, California: Seismic characterization of the magmatic system, *J. Geophys. Res.* **119,** 4907–4922.

Zinke, R., J. Hollingsworth, and J. F. Dolan (2014). Surface slip and off-fault deformation patterns in the 2013 M_w 7.7 Balochistan, Pakistan earthquake: Implications for controls on the distribution of near-surface coseismic slip, *Geochem. Geophys. Geosys.* **15,** 5034–5050.

Ziv, A., and A. Rubin (2000). Static stress transfer and earthquake triggering: No lower threshold in sight? *J. Geophys. Res.* **105,** 13,631–13,642.

Manuscript received 4 February 2020
Published online 30 June 2020